Title:

Identifying dynamic protein and RNA proximity interaction networks of actinin reveals RNA-binding and metabolic regulatory mechanisms

Feria A. Ladha M.S.[1], Ketan Thakar Ph.D.[2]*, Anthony M. Pettinato B.S.[1]*, Nicholas Legere B.S.[2], Rachel Cohn M.S.[2], Robert Romano B.S.[1], Emily Meredith B.S.[1], Yu-Sheng Chen Ph.D.[2], and J. Travis Hinson M.D.[1,2,3]

Affiliations:

[1]University of Connecticut Health Center, Farmington, CT 06030, USA

[2]The Jackson Laboratory for Genomic Medicine, Farmington, CT 06032, USA

[3]Cardiology Center, UConn Health, Farmington, CT 06030, USA

*These authors contributed equally

Lead Contact: Correspondence: travis.hinson@jax.org

Abstract

Actinins are actin cross-linkers that are expressed in nearly all cells and harbor mutations in heritable diseases. We deployed proximity-dependent biotinylation to identify actinin proximity proteins and RNA transcripts in human cardiomyocytes to reveal new functions of the actin cytoskeleton. We identified 285 proximity protein partners including unexpected effectors of RNA-binding and metabolism, and interrogated dynamic partners using a sarcomere assembly model. Mammalian two-hybrid studies established that IGF2BP2, an RNA-binding protein associated with type 2 diabetes, interacted with the rod domain of actinin through its K Homology domain. This interaction was necessary for actinin localization and translation of electron transport chain transcripts, and oxidative phosphorylation. Diminished IGF2BP2 in cardiac microtissues impaired contractile function in accord with diminished metabolic functions. This actinin proximity protein and RNA study expands our functional knowledge of the actin cytoskeleton, and uncovers new modes of metabolic regulation through interactions with RNA-binding proteins.

Main

Actinin proteins are ubiquitous spectrin family members that cross-link actin, and are important for a myriad of cellular functions including cell adhesion, migration, contraction, and signaling[1]. The four human actinin isoforms have distinct expression profiles (non-muscle *ACTN1* and *ACTN4*; cardiac muscle *ACTN2*; and skeletal muscle *ACTN3*), but share homologous amino acid sequences that are organized into three structural domains—an actin-binding (AB) domain composed of two calponin-homology domains, a central rod domain containing four spectrin-like repeats (SR), and a calmodulin-like domain (CaM) containing two EF hand-like motifs[2]. While it is thought that actinin evolved initially to regulate the early eukaryotic actin-based cytoskeleton[3], it has acquired more elaborate functions in vertebrates, including a mechanical role in the sarcomere, a specialized contractile system required for striated muscle function[3, 4]. Moreover,

normal actinin function is critical for multiple human organ systems as inheritance of *ACTN1*, *ACTN2*, and *ACTN4* mutations have also been linked to congenital macrothrombocytopenia, hypertrophic cardiomyopathy, and focal segmental glomerulosclerosis of the kidney, respectively[5-7].

In the cardiac sarcomere, alpha actinin-2 (referred henceforth as actinin) is the major structural component of the Z-disk, where it is essential for sarcomere assembly and function[8]. Actinin regulates sarcomere assembly by providing a scaffold for protein-protein interactions (PPIs) such as with titin (TTN) and actin through CaM and AB domains, respectively[8-10]. Secondary to these interactions, the thin and thick filament sarcomere systems are organized to promote twitch contraction. It has also been observed that while the Z-disk is one of the stiffest sarcomere structures, actinin demonstrates remarkably dynamic and complex molecular interactions such as with the actin cytoskeleton that are necessary for normal myocyte function[11]. Moreover, actinin interaction partners have also been described to exit the sarcomere to execute critical roles in mechanotransduction signaling, protein homeostasis and transcriptional regulation[12]. Secondary to the vast repertoire and dynamics of actinin molecular partners, there remain extensive gaps in our knowledge of not only how actinin regulates sarcomere assembly and function, but also within other cellular contexts enriched for actinin expression such as at focal adhesions and cell surface receptors in both striated and non-striated cells that may inform how actinin mutations cause human disease[13, 14].

Here, we comprehensively identified the actinin protein interactome in CRISPR/Cas9-engineered human cardiomyocytes using proximity-dependent biotinylation (BioID). This study utilizes cardiomyocytes (iPSC-CMs) differentiated from induced pluripotent stem cells (iPSCs) that express actinin fused to the promiscuous biotinylating enzyme BirA* from the *ACTN2* locus to provide *in vivo* actinin expression levels and localization[15]. We identify a high-confidence list of actinin neighborhood proteins including those that are dynamically regulated by sarcomere assembly to reveal molecular insights into this process as well other cytoskeletal functions. Our

study uncovers unexpected actinin interactions with a cluster of RNA-binding proteins including IGF2BP2, which enabled us to study RNA neighborhoods in actinin proximity, and to uncover new crosstalk between the actin cytoskeleton and oxidative phosphorylation that we find critical to cardiomyocyte contractile function. Our study also provides a list of molecules that can be studied to reveal insights into actin cytoskeletal dynamics and unexpected functions of actinin.

Results

BioID to identify actinin proximity partners

Actinin is an integral member of the actin cytoskeleton where it interacts within multiprotein complexes with diverse biophysical properties such as within Z-disks and membrane-associated focal adhesions, which are also dynamically regulated (Fig. 1a). Secondary to these actinin properties, we selected the method of BioID that has been shown to be effective within these contexts[16]. BioID uses BirA*, which is a genetically-modified version of *E. coli* BirA that enables promiscuous lysine biotinylation within ~10 nm radius of expression (Fig. 1b)[17].

We employed a genome engineering strategy to fuse BirA* with a hemagglutinin (HA) epitope tag to the carboxyl-terminus of endogenous *ACTN2* (Actinin-BirA*) in a human iPSC line using CRISPR/Cas9-facilitated homologous recombination (extended data Fig. 1a). We then selected and expanded an iPSC clone that expressed Actinin-BirA* fusion protein in directly-differentiated iPSC-CMs (Fig. 1c)[18, 19]. To first verify that Actinin-BirA* functioned similarly to unmodified actinin, we studied 3-dimensional cardiac microtissue assays that we previously utilized to test variants in sarcomere genes that cause heart failure[20, 21]. Unlike cardiac microtissues with heart failure-associated mutations, twitch force was unaltered by Actinin-BirA* expression (extended data Fig. 1b). We confirmed appropriate localization of Actinin-BirA* to the Z-disk by both co-localization immunofluorescence (Fig.1d) and HA-immunoprecipitation assays (Fig.1e). Actinin-BirA* interacted with the Z-disk protein titin-cap (TCAP), but not the sarcomere M-line protein myomesin[22-25], which supported appropriate localization. With the knowledge that

Actinin-BirA* functions similarly to unmodified actinin, we next optimized biotin supplementation conditions in iPSC-CMs and confirmed that optimal labeling is achieved after 50 μM biotin supplementation for 24 hours (Fig.1f, extended data Fig. 1c). Under these conditions, actinin-BirA* biotinylated targets that overlapped actinin localization in iPSC-CMs (Fig.1d), and demonstrated abundant protein biotinylation compared to controls (Fig. 1g).

To identify and quantify actinin proximity proteins, we subjected both biotin-pulsed control and Actinin-BirA* iPSC-CM lysates to streptavidin immunoprecipitation and tandem mass tags (TMT) quantitative proteomics (Fig. 1f). TMT of Actinin-BirA*- and control-precipitated proteins analyzed using hierarchical clustering and heatmap analysis (Fig.1h) demonstrated both low inter-replicate variability, and 285 high-confidence actinin proximity partners (extended data Table 1 and 2). The proximity list was next examined using Search Tool for the Retrieval of Interacting Genes/Proteins (STRING)[26] network analysis (extended data Fig. 1d). STRING confirmed identification of previously-known direct actinin interaction partners localized to the Z-disk including TTN[10], TCAP[10] and myozenin 2 (MYOZ2)[27] (Fig. 1i), which also belonged to a sarcomere cluster including numerous other sarcomere components determined by Gene-Ontology (GO) enrichment analysis. Actinin network proteins were also enriched within a focal adhesion cluster including previously-known direct actinin partner zyxin (ZYX)[28] (Fig.1j), and a cell junction (Fig. 1k) cluster that includes the previously-known actinin direct partner catenin alpha 1 (CTNNA1)[29]. BioID also uncovered less well-described actinin proximity network clusters including metabolism (Fig. 1l), mitochondrial membrane (Fig. 1m) and RNA-binding (Fig. 1n).

Actinin proximity partners change with sarcomere assembly

During sarcomere assembly, actinin first organizes into punctate Z-bodies, or pre-myofibrils, that coalesce to form striated Z-disks[30], and this assembly process, though critical to cardiomyocyte contractile function, is incompletely understood. As it has been previously observed that cardiomyocytes that lack troponin T (cTnT; encoded by *TNNT2*) only assemble Z-bodies[31], we

studied cTnT knockout (KO) and wildtype (WT) iPSC-CMs as a model to understand actinin proximity partners through two stages of sarcomere assembly. We started by inserting a homozygous cTnT-KO mutation into the Actinin-BirA* iPSC line using CRISPR/Cas9 and error-prone non-homologous end joining repair. We verified that cTnT-KO iPSC-CMs expressed no cTnT protein (extended data Fig. 2a), and actinin antibodies only decorated Z-body structures (Fig. 2a). We then performed TMT, and compared actinin proximity partners in cTnT-WT to cTnT-KO iPSC-CMs (extended data Fig. 2b). Overall, sarcomere assembly enhanced actinin interactions as we observed an increase in the relative intensity values for cTnT-WT relative to both cTnT-KO and control samples (Fig. 2b). Next, we examined actinin proximity partners by their dependence on sarcomere assembly (Fig. 2c, extended data Table 3). We first tested a prevailing sarcomere assembly hypothesis that non-muscle myosin isoforms localize to Z-bodies, and are subsequently replaced by muscle myosin isoforms in Z-disks[30]. Our results are consistent with this model as actinin proximity with cardiac muscle beta isoform (MYH7) increased by 89% with Z-disk assembly in cTnT-WT iPSC-CMs, while non-muscle type B isoform (MYH10) exhibited a negligible 4% increase. Overall, we identified 80 sarcomere assembly-dependent actinin proximity partners that clustered into GO terms for "sarcomere", "unfolded protein response", "translation", "glycolysis" and "mitochondrial membrane" (Fig. 2d).

Sarcomere assembly-dependent actinin interactions also demonstrated a shift from proximity partners localized in focal adhesions to the sarcomere. For example, the most sarcomere assembly-dependent enrichment partner (123% increase) was cysteine and glycine rich protein 3 (CSRP3) (Fig. 2c). CSRP3 is a Z-disk protein that has been implicated to regulate mechanical stretch signaling[32], anchor calcineurin to the sarcomere[33], and cause heart failure when mutated[34]. In contrast, focal adhesion components including talin 2 (TLN2) were depleted (12% decrease) from actinin proximity (Fig. 2c). Sarcomere assembly also enhanced actinin proximity partners with metabolic functions and with mitochondrial membrane localizations, which suggested that spatial regulation of these co-localized modules may be important in

metabolic regulation (Fig. 2d). In support of this, sarcomere assembly increased mitochondrial content (extended data Fig. 2c) and oxygen consumption rates (extended data Fig. 2d, 2e). In summary, sarcomere assembly shifted actinin proximity partners from focal adhesions to the sarcomere; differentially-regulated muscle and non-muscle myosins; co-localized mitochondrial membrane, metabolic and translational factors; and increased oxidative metabolism.

RIP-seq to identify actinin proximity RNA transcripts

We next sought to identify actinin proximity RNA transcripts that could reveal insights into new actinin functions in RNA biology. With new knowledge of actinin proximity partners that bind RNA (Fig.1n), and with Actinin-BirA* iPSC-CMs that could enable indirect RNA transcript precipitation through affinity purification of biotinylated RNA-binding proteins using streptavidin, we performed a modified version of RNA immunoprecipitation followed by sequencing (RIP-seq) (Fig. 3a)[35]. Principle component analysis (PCA) of RIP-seq data demonstrated distinct clustering of Actinin-BirA* samples compared to controls (Fig. 3b), and differential expression analysis identified 945 transcripts that were actinin proximity-enriched. GO analysis (Fig. 3c) revealed overwhelming enrichment of transcripts encoding electron transport chain (ETC) proteins (Fig. 3d, extended data Fig. 3a). In contrast, we found no actinin enrichment for glycolysis transcripts (Fig. 4e, extended data Fig. 3b). 1113 transcripts were actinin proximity-depleted, while GO terms revealed functions in chromatin and the nucleus (Fig. 3c). Cytoskeletal transcripts including those encoding sarcomere thin and thick filament proteins were surprisingly depleted (Fig.3f, extended data Fig. 3c) from actinin proximity despite their proteomic enrichment.

Following qPCR validation of RIP-seq hits (extended data Fig. 3d), we performed RNA fluorescence *in situ* hybridization (RNA FISH) to confirm ETC transcript localization relative to actinin protein expression. Actinin protein co-localized with transcripts encoding *NDUFA1*, an ETC complex I component, but not *TTN* (Fig. 3g, 3h). We also validated two additional actinin protein-enriched transcripts including *NDUFA8* and *GPX4* (Fig. 3h). We next assessed for *NDUFA1* and *NDUFA8* transcript co-localization, which could reflect ETC transcript storage or

processing mechanisms. While both *NDUFA1* and *NDUFA8* transcripts localized near actinin protein, they did not overlap (extended data Fig. 3e).

With knowledge of actinin-localized transcripts, we next performed polysome profiling (Fig. 3i) followed by sequencing (Polysome-seq)[36] to understand if actinin proximity localization related to translation. PCA analysis demonstrated tight clustering of replicates of polysome-bound transcripts compared to controls (Fig. 3j), and 273 transcripts were shared between the polysome- and actinin protein-enriched fractions (Fig. 3k). Shared transcripts represented 28.9% of total actinin protein-enriched transcripts, and 24.7% of total polysome-enriched transcripts. GO term analysis of overlapped transcripts revealed mitochondrial functions, which was particularly prominent for ETC complex members (Fig. 3l, extended data Fig. 3f). Conversely, actinin proximity-depleted but polysome-enriched transcripts enriched for distinct GO terms including ribosome and troponin complex (Fig. 3l, extended data Fig. 3g).Together, these data provide evidence that actinin functions as a PPI hub by co-localizing mitochondrial membrane, RNA-binding, and translational proteins with transcripts involved in oxidative phosphorylation.

IGF2BP2 binds actinin rod domains through K homology domains

Direct actinin interactions with RNA-binding proteins have not been previously well-described, but this knowledge could provide new mechanisms of RNA regulation. Because ETC transcripts were in proximity to actinin, we focused our study on candidate actinin-interacting RNA-binding proteins secondary to their association with metabolic functions in the literature including IGF2BP2[37], PCBP1[38], PCBP2[39], and SERBP1[40]. We first confirmed actinin proximity results using streptavidin affinity purification followed by immunoblotting against the four RNA-binding proteins (Fig. 4a, extended data Fig. 4a). We also co-immunoprecipitated Actinin-BirA* using an HA epitope antibody and found supportive evidence that IGF2BP2, PCBP1 and PCBP2 physically interacts with actinin (Fig. 4b, extended data Fig. 4b). The lack of SERBP1 co-immunoprecipitation suggested a more complex interaction mechanism.

To extend co-immunoprecipitation results, we also tested the mode of interaction between actinin and IGF2BP2, PCBP1, PCPB2, and SERBP1 using mammalian 2-hybrid (M2H) assays. We began by constructing expression vectors encoding full-length or structural domains of actinin and RNA-binding proteins. M2H using IGF2BP2 as “prey” and full-length actinin as “bait” resulted in luciferase activation, but not for PCBP1, PCBP2 or SERBP1 (Fig. 4c, extended data Fig. 4c). We expanded our M2H study to evaluate other actinin isoforms (*ACTN1-4*), and all muscle and non-muscle isoforms interacted with IGF2BP2 illustrating that this interaction is a general feature of all actinins (extended data Fig. 4e). We next mapped the IGF2BP2-actinin interaction to IGF2BP2’s K Homology (KH) structural domain but not its RNA recognition motif (RRM). Using IGF2BP2 as “bait”, we then mapped the actinin-binding site to its rod domain (Fig. 4d). In support of these findings, we observed co-localization of IGF2BP2 with actinin by immunofluorescence, which was especially prominent at Z-disks (Fig. 4e). These data (extended data Fig. 4d) both validate our BioID results that implicate actinin as an interaction hub for RNA-binding proteins, and establish that IGF2BP2 directly binds actinin through specific structural domains.

IGF2BP2 localizes ETC transcripts to actinin, which promotes ETC function and cardiomyocyte contraction

IGF2BP2 has been shown to bind ETC transcripts in glioblastoma stem cell lines[41], and this observation provided the rationale to test whether IGF2BP2 could also be responsible for actinin-localization of ETC transcripts. We employed a genetic knockdown approach using an shRNA that decreased IGF2BP2 protein levels in iPSC-CMs (Fig. 5a), and performed RIP-qPCR in IGF2BP2-depleted iPSC-CMs to quantify actinin-localized ETC transcripts including *NDUFA1*, *NDUFA8*, *NDUFA11*, and *COX6B1*. IGF2BP2 knockdown decreased these actinin-localized transcripts (Fig. 5b) but not total cellular transcript levels (Fig. 5c)—clarifying that IGF2BP2 is necessary for actinin proximity localization but not stability. Because not all IGF2BP2 is in proximity to actinin (Fig. 4e), and IGF2BP2 may have other functions, we

sequentially precipitated transcripts by IGF2BP2 antibody first to collect all IGF2BP2-bound transcripts, followed by streptavidin affinity to study the subset of IGF2BP2-bound transcripts that are in actinin proximity (extended data Fig. 5a). We confirmed ETC transcript enrichment at actinin-localized IGF2BP2 (extended data Fig. 5a).

Because ETC transcripts were actinin-localized by IGF2BP2, and these transcripts were polysome-enriched, we hypothesized that IGF2BP2 genetic knockdown could impair ETC transcript translation and ETC function. To test this, we measured protein levels of subunits from ETC complexes I-V as well as a glycolytic control, GAPDH. IGF2BP2 knockdown resulted in diminished protein expression across all ETC complexes, but not GAPDH (Fig. 5d). Functionally, IGF2BP2 depletion resulted in reduced mitochondrial content (Fig. 5e) and oxygen consumption rates (Fig. 5f, 5g), which would be consistent with reduced ETC translation. Because cardiomyocytes utilize oxidative metabolism for energy production[42], we hypothesized that IGF2BP2 knockdown could impair iPSC-CM functions especially ATP-consuming pathways such as sarcomere contraction. To test contractile function, we knocked-down IGF2BP2 using an shRNA and produced cardiac microtissues (Fig. 5h). In accord with diminished oxidative metabolism, and the energy-dependence of contraction, IGF2BP2 knockdown resulted in decreased twitch contraction (Fig. 5i). To confirm that diminished contraction was not secondary to translational changes in contractility proteins, we quantified beta myosin heavy chain (β-MHC) and troponin I (TnI) levels. Levels of both contractile proteins were unchanged (Fig. 5j). We conclude that IGF2BP2 transports ETC transcripts to the actin cytoskeleton through direct physical interactions with actinin, which supports translation of ETC transcripts, oxidative phosphorylation and contractile function. We propose that IGF2BP2, in partnership with additional actinin-localized factors that regulate RNA-binding, translation and metabolism, form a subcellular spatial hub that links the actin cytoskeleton to metabolic regulation (Fig. 5k).

Discussion

The actinins are multipurpose actin cross-linkers that execute their tasks through PPIs with a myriad of partners with diverse biophysical properties and kinetics including the sarcomere, adhesion sites, and transmembrane receptors. Robust methods are necessary to understand the identities, organization and functions of these distinct actin cytoskeletal PPI hubs. Here, we examined the actinin interaction network using proximity-dependent biotinylation by BioID. The vast number of actinin interactions identified in our study was made possible by the unique capabilities of BioID including the ability to detect both direct and vicinal interactions, static and dynamic interactions and interactions in diverse microenvironments such as with membrane-associated partners. In contrast, many actinin PPI studies have utilized yeast two-hybrid approaches that can be challenging with proteins that dimerize and can self-activate yeast reporters[43]. The robustness of our interaction study was achievable through fusion of BirA* into the endogenous actinin locus made possible with CRISPR/Cas9, which led to Actinin-BirA* expression levels and localization that mimicked unaltered actinin. By targeting the endogenous genetic locus, our approach could also be extended to studies of particularly large proteins including other spectrin family proteins, or to other cell lineages differentiated from iPSCs to understand cell type-specific PPIs.

A major objective of this study was to determine the molecular composition of the Z-disk through sarcomere assembly. Our current understanding of Z-disk proteins is derived from stitching together smaller PPI studies focused usually on a single interaction, but has not been systematically characterized especially through a dynamic process such as sarcomere assembly. Here, we combined BioID with a two-stage sarcomere assembly model (i.e. Z-body and Z-disk) and confirmed previous Z-disk proteins including TTN[10], TCAP[27], LDB3[44], MYOZ2[27] and CSRP3[33]. CSRP3 was the most-enriched actinin proximity partner with sarcomere assembly, which suggests that CSRP3 may regulate Z-disk organization. While this will require additional studies, it is consistent with observations made by others in mice that CSRP3 genetic disruption impairs Z-disk architecture and results in heart failure[45]. In addition to sarcomere

components, we observed sarcomere assembly-dependent interaction partners in functional modules of glycolysis, translation, unfolded protein response, NAD/NADH binding and localization to mitochondrial membranes. Muscle actinin isoforms have been previously found to interact with enzymes related to glucose metabolism including glycogen phosphorylase[46], aldolase[47] and fructose-bisphosphatase[47]. Our study confirms actinin-proximity with glycogen phosphorylase (PYGM and PYGB), but also provides a list of additional glycolytic interaction partners including clarifying those that are sarcomere assembly-dependent such as the rate-limiting glycolytic enzyme phosphofructokinase (PFKM). Actinin proximity of PFKM may regulate glucose metabolism through post-translational mechanisms that remain to be explored. In the future, our study could be extended to employ more dynamic approaches such as with the recently-described TurboID enzyme[48], which exhibits vastly-improved biotinylation kinetics (~15mins) and labeling efficiencies compared to BirA*.

Our BioID study yielded unexpected actinin functions in spatial regulation of RNA localization and translation. In zebrafish, 71% of transcripts are localized in spatially-distinct patterns[49], which provides spatial and temporal regulation of gene expression such that local stimuli can regulate translation on-site[50]. We find that actinin serves as a PPI hub for RNA-binding proteins and translational machinery, which we exploited to identify actinin-localized transcripts that function in the ETC. Our study provides potential new mechanisms for the previous observation that intermyofibrillar mitochondria both reside adjacent to the Z-disk[51], and have higher rates of oxidative phosphorylation[52]. We find that ETC transcript localization to actinin is dependent on interactions with IGF2BP2, an RNA-binding protein associated with type 2 diabetes by genome-wide association studies[37]. In our study, IGF2BP2 knockdown using a 3-dimensional cardiac microtissue model resulted in diminished contractile function in association with reduced ETC translation and oxygen consumption rates. This mechanism may inform why IGF2BP2 knock-out mice also have impaired fatty acid oxidation in skeletal muscle where actinin is also highly expressed[53]. Finally, our combined proximity proteomic and RNA study

provides unexplored areas for investigation for the research community to continue to explore and refine actinin functions.

Acknowledgements

This study could not have been completed without the assistance of Bo Reese (UConn Center for Genome Innovation) for RNA sequencing and RIP-seq, and Anthony Carcio (The Jackson Laboratory for Genomic Medicine) for flow cytometry. TMT proteomics and quantitative analyses was supported by Sanjukta Thakurta from the Thermo Fisher Center for Multiplexed Proteomics at Harvard Medical School. Artwork was created using BioRender. Funding for this study was obtained from the National Institutes of Health (J.T.H., HL125807, HL142787, and EB028898), American Heart Association (F.A.L., PRE35110005, and A.M.P., PRE34381021) and institutional start-up funds (UConn Health).

Author Contributions

Investigation and Validation, F.A.L., A.M.P., K.T., N.L., and J.T.H.; Cells and/or reagent generation, F.A.L., A.M.P., K.T., N.L., R.C., R.R., E.M., Y.S.C., and J.T.H.; Formal Analysis, F.A.L., A.M.P., and J.T.H.; Funding Acquisition, F.A.L., A.M.P., and J.T.H.; Conceptualization and Supervision, J.T.H; Writing, F.A.L., A.M.P., and J.T.H.

Figure legends:

Figure 1. Actinin proximity interaction networks using BioID. a) Overview of actinin localization in cardiomyocytes including sarcomere Z-disk, focal adhesion and cortical actin cytoskeleton. **b)** Overview of the BioID method using Actinin-BirA* fusion to study actinin proximal protein networks. **c)** iPSC-CM lysates were probed with anti-actinin and anti-GAPDH to identify Actinin-BirA* fusion (~130kD) and endogenous actinin (~100kD). **d)** Confocal micrograph of Actinin-BirA* iPSC-CMs decorated with antibodies to actinin (red), streptavidin-

AF488 (green) and DAPI DNA co-stain (blue) (scale bars, main image-10μm, inset-5μm). **e)** To validate localization, iPSC-CM lysates were immunoprecipitated with an anti-HA antibody, and probed with antibodies to known sarcomere components at Z-disk (anti-TCAP) and M-line (anti-myomesin), as well as anti-HA and anti-actinin controls. **f)** Overview of BioID experimental methods. **g)** iPSC-CM lysates were probed with streptavidin-HRP to examine Actinin-BirA*-biotinylated proteins. **h)** TMT quantitative data illustrated using hierarchical clustering and heatmap confirms low inter-replicate variability and 285 Actinin-BirA*-enriched proteins. **i-n)** Interaction maps of TMT results based on STRING and GO terms – sarcomere, focal adhesion, cell junction, metabolism, mitochondrial membrane, and RNA-binding. ACTN2 was shaded red to recognize established network interactions (i, j).

Figure 2. Sarcomere assembly-dependent actinin proximity interaction networks. a) Confocal micrograph of cTnT-KO Actinin-BirA* iPSC-CMs decorated with antibodies to actinin (red), streptavidin-AF488 (green), and DAPI DNA co-stain (blue) (scale bars, main image-10μm, inset-5μm). In contrast to the Z-disks observed in cTnT-WT iPSC-CMs (fig. 1d), cTnT-KO iPS-CMs have punctate Z-bodies. **b)** TMT quantitative data illustrated using hierarchical clustering and heatmap for two-stage sarcomere assembly reveal 80 sarcomere assembly-dependent actinin proximity partners (>30% increase in intensity in cTnT-WT compared to cTnT-KO samples). **c)** List of actinin proximity partners organized by fold-change enrichment with sarcomere assembly. **d)** STRING interaction map of sarcomere assembly-dependent TMT results analyzed by cluster analysis reveals five clusters labeled by GO enrichment terms.

Figure 3. Identifying actinin-localized RNA transcripts using RIP-seq. a) Overview of modified RIP-seq protocol to study actinin proximity RNA transcripts by streptavidin affinity purification of RNA-binding proteins followed by RNA isolation and sequencing. **b)** PCA plot shows clustering of Actinin-BirA* RIP-seq samples relative to controls (n=4). **c)** Volcano plot of RIP-seq data shaded red for 945 actinin-enriched transcripts (FDR <0.05, L2FC ≥0.5) and blue

for 1113 actinin-depleted transcripts (FDR <0.05, L2FC ≤-0.5). Differentially-enriched transcripts were analyzed by GO and enrichment terms are listed for actinin-enriched or actinin-depleted samples. **d)** ETC gene components spanning respiratory chain complex I-V proteins are actinin proximity-enriched on average. Each unshaded circle represents a single ETC gene. **e)** Glycolysis gene components are not actinin proximity-enriched on average. Each unshaded circle represents a single glycolysis gene. **f)** Sarcomere gene components divided by localization to the thick or thin filament are not actinin proximity-enriched or are depleted on average, respectively. Each unshaded circle represents a single sarcomere gene. **g)** Representative confocal micrograph of iPSC-CMs decorated with antibodies to actinin (red), DAPI DNA co-stain (blue), and RNA FISH probes against *NDUFA1* (green) and *TTN* (purple). (scale bars, main image-10μm, inset-5μm). **h)** Quantification of RNA proximity to actinin. Data are derived from n=10 cells. **i)** Representative polysome profile of iPSC-CMs used for Polysome-seq studies. **j)** PCA plot shows clustering of polysome-enriched transcripts compared to controls. **k)** Venn diagram illustrating unique and overlapping transcripts between Actinin-BirA* RIP-seq and Polysome-seq (FDR <0.05, -0.5 ≤ L2FC ≥ 0.5 for both). **L)** Overlay of Actinin-BirA* RIP-seq and Polysome-seq results to identify actively translating genes (FDR <0.05, L2FC ≥0.5 by Polysome-seq) that are actinin proximity-enriched (FDR <0.05, L2FC ≥0.5 by RIP-seq), or actinin proximity-depleted (FDR <0.05, L2FC ≤-0.5 by RIP-seq) and the resulting GO terms for each gene set. Data are mean ± SEM; significance assessed by one-way ANOVA using Holm-Sidak correction for multiple comparisons (h).

Figure 4. RNA-binding protein IGF2BP2 directly binds actinin. a) Representative immunoblot probed with antibodies to IGF2BP2 in streptavidin affinity-purified lysates. Double band represents two IGF2BP2 splice products. **b)** Representative immunoblot probed with antibodies to IGF2BP2 in anti-HA immunoprecipitated lysates. Double band represents two IGF2BP2 splice products. **c)** Mammalian-two-hybrid (M2H) study conducted in 293T cells to fine map the direct interaction between actinin and IGF2BP2. IGF2BP2 was divided into RRM

(residues 1-160) and KH (residues 161-600) domains to fine-map the interaction. All data are n=3. The statistical significance was calculated by a paired two-tailed t-test **d)** M2H results to fine map the direct interaction between the KH domain of IGF2BP2 and Actinin. Actinin was divided into AB (residues 1-275), rod (residues 276-750) and CaM domains (residues 751-895). All data are n=3. **e)** Representative confocal micrograph demonstrating partial co-localization of actinin (anti-actinin; red) with IGF2BP2 (anti-IGF2BP2; green) with DAPI DNA (blue) co-stain in iPSC-CMs. (scale bars, main image-10μm, inset-5μm). Data are mean ± SEM; significance assessed by one-way ANOVA using Holm-Sidak correction for multiple comparisons (c, d) and defined by $P \leq 0.0001$ (****).

Figure 5. IGF2BP2 localizes ETC transcripts to actinin, and promotes ETC translation and cardiac microtissue contraction. a) Representative immunoblot of lysates from iPSC-CMs treated with shRNA targeting IGF2BP2 or scramble control probed with antibodies to IGF2BP2 and GAPDH. Double band represents two IGF2BP2 splice products. **b)** Streptavidin affinity purification of transcripts bound to actinin proximity-enriched targets after IGF2BP2 knockdown, followed by qPCR of ETC transcripts *NDUFA1*, *NDUFA8*, *NDUFA11* and *COX6B1*. **c)** QPCR analysis of global transcript levels of *NDUFA1*, *NDUFA8*, *NDUFA11* and *COX6B1* after IGF2BP2 knockdown. **d)** Representative immunoblot of lysates from iPSC-CMs after IGF2BP2 knockdown, and probed with antibodies to ETC complex I-V subunits (anti-ATP5A, UQCRC, MTCO1, SDHB and NDUFB8), IGF2BP2 and GAPDH control. **e)** FACs analysis of iPSC-CMs stained with MitoTracker after IGF2BP2 knockdown (N>5000 events per replicate). **f)** Oxygen consumption rates normalized to protein levels after IGF2BP2 knockdown in iPSC-CMs, and **(g)** specific OCR parameter quantification. **h)** Overview of cardiac microtissue platform and twitch force analysis. ECM-extracellular matrix slurry. Fibroblasts-normal human ventricular fibroblasts. (scale bar-150μm). **i)** Cardiac microtissues exhibit reduced twitch force after IGF2BP2 knockdown. Data are n≥10 microtissues. **j)** Representative immunoblot of lysates from iPSC-

CMs probed with antibodies to myosin heavy chain 7 (β-MHC) and troponin I (TnI) proteins show no change in expression despite IGF2BP2 knockdown. Anti-GAPDH used as additional control. **k)** Proposed model of an actinin-based PPI hub that promotes localized oxidative phosphorylation (OXPHOS) through proximity interactions with RNA binding proteins (RBP) including IGF2BP2, translational machinery, unfolded protein response (UPR), and mitochondria. Data are n≥3; mean ± SEM; significance assessed by Student's t-test (a-e, g, i, j) and defined by $P \leq 0.05$ (*), $P \leq 0.01$ (**).

Materials and Methods

iPSC Culture and iPSC-CM Differentiation

All stem cell experiments were done in PGP1 iPSCs (Coriell #GM23338), which have been extensively characterized including whole genome sequencing and karyotyping as part of the ENCODE project (ENCBS368AAA). iPSCs were maintained on Matrigel-coated tissue culture plates (Corning 354230) in mTeSR1 (STEMCELL Technologies 85875). iPSCs were passaged at 80-90% confluency utilizing Accutase (BD 561527) and 10 μM ROCK inhibitor Y-27632 (Tocris 1254). iPSC-CMs were directly differentiated by sequential modulation of Wnt/β-catenin signaling, as previously described[21, 54]. On Day 13 of differentiation, iPSC-CMs were purified by metabolic enrichment using glucose-free DMEM (Gibco 11966025) supplemented with 4 mM lactate (Sigma 71718) for 24-48 hours[18]. Following selection, iPSC-CMs were trypsinized (Gibco 25200056) and re-plated onto fibronectin-coated tissue culture plates (Gibco 33016015). IPSC-CMs were maintained in RPMI-B27. For proximity-labeling experiments, control and Actinin-BirA* iPSC-CMs were maintained in DMEM (Gibco 11965092) supplemented with homemade biotin-free B27 following metabolic enrichment[55, 56]. For BioID studies, control and Actinin-BirA* iPSC-CMs were treated with 50 μM biotin for 24 hours followed by a 2-hour washout phase in biotin-free media before collection. All iPSC-CM analyses were performed on Day 25-30 unless noted otherwise.

Plasmid Cloning

The homologous recombination (HR) targeting vector (System Biosciences HR220PA-1) was modified prior to being used in genome-editing experiments. A gene fragment for BirA* (R118G)-HA tag was obtained (IDT) and cloned into the parent vector via Gibson assembly (NEB E2621). *ACTN2* ~800bp 5' and 3' HR arm gene fragments (IDT) were then cloned into the appropriate cloning sites (sequences in Table S5). All HR vector propagation steps were performed in DH5α *E.coli* (NEB C2987). For hairpin (shRNA) experiments, the pLKO.1 puro lentiviral plasmids containing either shScramble (Addgene 1864) or shIGF2BP2 (sequence in Table S5) were assembled using T4 DNA ligase (NEB M0202S) and propagated in NEB Stable *E.coli* (NEB C3040).

CRISPR/Cas9 studies

Genome editing was performed utilizing a CRISPR/Cas9 protocol adapted from previous studies[20, 21]. $8x10^6$ iPSCs were electroporated with 20 µg pCas9-GFP (Addgene 44719), 20 µg of the appropriate hU6-driven sgRNA (designed using crispr.mit.edu), and 20 µg of the HR targeting vector to generate *ACTN2-BirA** knock-in iPSCs. Electroporated cells were transferred to a Matrigel-coated 100 mm dish containing mTeSR1 and 10 µM Y-27632. The following day, selection was started with 50 µg/mL Hygromycin B (Invitrogen 10687010) to isolate single iPSC clones, which were then manually picked, expanded, and screened via Sanger sequencing. Isogenic knockout of *TNNT2* was performed similarly, but in the absence of an HR vector and with GFP-based FACS enrichment in place of antibiotic selection.

Immunoprecipitation Experiments

Streptavidin immunoprecipitation

After biotin washout, control and Actinin-BirA* iPSC-CMs were rinsed three times with room temperature PBS. Cells were lysed with lysis buffer (50 mM Tris-Cl pH7.4, 500 mM NaCl, 0.2% SDS, 1x protease inhibitor, 1mM DTT, ddH_2O). Lysates were sonicated (Branson 250) two times on ice with 2 minutes between each cycle (30 pulses, 30% duty cycle, output level3).

Samples were centrifuged to pellet cell debris and cleared lysate were added to magnetic Dynabeads MyOne Streptavidin C1 beads (Invitrogen 65001), which were prewashed with PBS and lysis buffer. Immunoprecipitation was performed on a rotator overnight at 4°C. The following day, the beads were resuspended in wash buffer 1 (2% SDS, ddH_2O), rotated for 8 minutes at room temperature, and then re-collected using a magnetic separation stand. The same steps were then repeated with wash buffer 2 (0.1% deoxycholic acid, 1% triton X-100, 1mM EDTA, 500 mM NaCl, 50 mM HEPES pH7.5, ddH_2O) and wash buffer 3 (0.5% deoxycholic acid, 0.5% NP-40, 1 mM EDTA, 250 mM LiCl, 10 mM Tris-Cl pH7.4, ddH_2O). Finally, the washed beads were resuspended in PBS, snap frozen, and sent for quantitative proteomics.

HA immunoprecipitation

Control and Actinin-BirA* iPSC-CMs were collected at Day 25 and HA-tag IP was conducted using reagents supplied in HA-tag IP/Co-IP Application set (Thermo Scientific 26180Y). The subsequent protein immunoblots were conducted as outlined in the immunoblot section.

RNA Immunoprecipitation (RIP)

After biotin washout, control and Actinin-BirA* iPSC-CMs were rinsed three times with room temperature PBS. Cells were lysed with ice-cold RIP buffer (150 mM KCl, 25 mM Tris-Cl pH7.4, 5 mM EDTA, 0.5 mM DTT, 0.5% NP40, 1x protease inhibitor, 100 U/ml RNase inhibitor, RNase-free water). Cell debris was pelleted and cleared lysate was added to magnetic Dynabeads MyOne Streptavidin C1 beads (Invitrogen 65001), which were prewashed with PBS and RIP buffer. Samples and beads were incubated on a rotator overnight at 4°C. The following day, the beads were washed three times with ice-cold RIP buffer – all steps were performed in a 4°C room. Samples were then incubated with Proteinase K at 55°C for 30 minutes. Beads were resuspended in TRIzol (Invitrogen 15596018), RNA extraction was performed immediately followed by RNA-sequencing.

Tandem Immunoprecipitation

After biotin washout, control and Actinin-BirA* iPSC-CMs were rinsed three times with room temperature PBS and then lysed in RIP buffer. Cleared lysates were incubated with Dynabeads Protein G (Invitrogen 10003D) pre-bound to either IgG antibody (MBL PM035) or IGF2BP2 antibody (MBL RN008P). Samples and beads were incubated on a rotator overnight at 4°C. The following day, the Protein G beads were washed three times with RIP buffer and then incubated for 12 hours with rotation at 4°C in RIP buffer containing IMP2 peptide (Genescript). The supernatant was then mixed with magnetic Dynabeads MyOne Streptavidin C1 beads (Invitrogen 65001), which were prewashed with PBS and RIP buffer. The following day, the streptavidin beads were three times washed with ice-cold RIP buffer – all steps were performed in a 4°C room. Samples were then incubated with Proteinase K at 55°C for 30 minutes. Beads were resuspended in TRIzol, RNA extraction was performed immediately followed by cDNA synthesis (outlined in Quantitative PCR section).

Quantitative proteomics

Bead digestion

After conducting streptavidin immunoprecipitation, streptavidin beads were snap frozen and sent to the Thermo Fisher Center for Multiplexed Proteomics (TCMP) at Harvard Medical School. There, beads were washed three times with 50 mM Tris buffer (pH 8.0) to remove any residual contents and resuspended in 1M Urea, 50 mM Tris (pH 8.0). An initial digest was performed for 1 hour at 37°C with Trypsin (5ng/ul), followed by brief centrifugation and supernatant collection. Beads were washed three time with 1M Urea, 50 mM Tris (pH 8.0), washed fractions were pooled, and digest was continued overnight at room temperature. The next morning, digested peptides were reduced with 5 mM TCEP, alkylation with 10 mM Iodoacetamide, quenching alkylation with 5 mM DTT, and final quenching with TFA. Stage-tip desalting on acidified digested peptides was conducted as previously described[57]. Peptide were eluted with 80% acetonitrile, 0.1% TFA and dried with speedvac. Dried desalted peptide samples were reconstituted with 200 mM EPPS buffer (pH 8.0) and labelled with first 9 of a 10-

plex tandem mass tag (TMT) reagent. 9-plex labeling reactions were conducted for 1 hour at room temperature. Modification of tyrosine residues with TMT was reversed with the addition of 5% hydroxyl amine for 15 minutes and the reaction was quenched with 0.5% TFA. Next, samples were combined, desalted over stage-tip, eluted into Autosampler Inserts, dried in a speedvac, and reconstituted in 5% acetonitrile-5% TFA for next steps.

Liquid chromatorgraphy-MS3 spectrometry (LC-MS/MS)

Labelled samples were analyzed on an Orbitrap Fusion mass spectrometer (Thermo Fisher Scientific) with a Thermo Easy-nLC 1200 for online sample handling and peptide separations[58]. Peptides were separated using a 180 min linear gradient from 5% to 42% buffer B (90% ACN + 0.1% formic acid) equilibrated with buffer A (5% ACN + 0.1% formic acid) at a flow rate of 500 nL/min across the column. MS1 data was collected in Orbitrap using a resolution of 120,000 with a scan range of 350-1350 m/z with a maximum injection time of 50 ms. MS2 analysis consisted of CID (quadrupole isolation set at 0.7 Da and ion trap analysis, AGC 9×10^3, Collision Energy 35%, maximum injection time 80 ms). The top ten precursors from each MS2 scan were selected for MS3 analysis (synchronous precursor selection), in which precursors were fragmented by HCD prior to Orbitrap analysis (Collision Energy 55%, max. AGC 1×10^5, maximum injection time 120 ms, resolution 50,000 and isolation window set to 1.2 – 0.8).

LC-MS3 data analysis

Uniprot Human database was used to search forward and reverse sequences of MS/MS spectra. The follow criteria were used: tryptic with two missed cleavages, a precursor mass tolerance of 50 ppm, fragment ion mass tolerance of 1.0 Da, static alkylation of cysteine (57.02146 Da), static TMT labeling of lysine residues and N-termini of peptides (229.162932 Da), and variable oxidation of methionine (15.99491 Da). Poor quality MS3 spectra were excluded from quantification (<200 summed signal-to-noise across 10 channels and <0.5 precursor isolation specificity).

Bioinformatics analysis

For analysis, raw intensity values underwent +1 correction prior to log transformation and subsequent enrichment analysis. Search Tool for the Retrieval of Interacting Genes/Proteins (STRING v. 11.0) was utilized for generation of interaction scores and Gene ontology (GO) term enrichment and KEGG Pathway analysis provided in supplemental tables. Cytoscape (v.3.7.2) was utilized to generate interaction maps with an organic layout and the utilization of the CLUSTER and BINGO features for group clustering and appropriate GO term identification for each cluster. Quantitative proteomics raw data deposited to the ProteomeXchange Consortium identifier PXD018040.

Quantitative PCR, RNA sequencing, and analysis

cDNA was synthesized using Superscript III First-Strand synthesis (Invitrogen 18080-400). Gene-specific PCR primers were designed or identified from the literature and transcripts were quantified using Fast SYBR Green (Applied Biosystems 4385612) on a ViiA7 Real-Time PCR system (Applied Biosystems).

RNA Samples were sent for sequencing at the University of Connecticut Institute for Systems Genomics. RNA sequencing libraries were generated using Illumina TruSeq Stranded Total RNA library preparation (Ribo-Zero depletion for rRNA was utilized for RIP-seq). Illumina NextSeq 500/550 sequencing was conducted with the v2.5 300 cycle reagent kit 9 (High Output). Estimated total single end reads per sample = 30-35M 150bp PE reads. Samples sequences were aligned with STAR to the hg38 human genome. In order to look at differential expression, DESeq2 (Bioconductor) was utilized. Gene Set Enrichment Analysis (GSEA) was utilized to determine GO terms for data sets. Top 10 GO terms are presented. Furthermore, for ETC complexes, glycolysis, and sarcomere gene sets – GSEA gene sets were utilized and those with an average ≥5 TPM value were included in the data set. Genome sequencing datasets are deposited at GEO under accession numbers: GSE144805 and GSE144806.

Protein Immunoblotting

Samples of interest were lysed in RIPA buffer (Cell Signaling 9806) containing protease inhibitor cocktail (Roche 11836170001), 1 mM PMSF, and phosphatase inhibitor (Pierce A32957), unless noted otherwise. Protein lysate concentrations were normalized using Pierce BCA (Thermo 23225), and then reduced and denatured in sample buffer (Thermo 39000). Lysates were separated on Bio-Rad 4–20% Mini-PROTEAN TGX precast gels, transferred via Bio-Rad Trans-Blot Turbo onto PVDF membranes (Bio-Rad 1704272), blocked in TBS-T (TBS with 0.1% Tween-20) containing 5% BSA, and probed overnight at 4°C with primary antibody. The next day, blots were washed in TBS-T and probed with HRP-linked secondary antibody (Cell Signaling 7076; 7074; Streptavidin-HRP 3999S) for 1 hour. Signal detection was performed using ECL substrate (Thermo 34577; 34095) and a Bio-Rad ChemiDoc MP imaging system. Blot images were digitally processed and analyzed in ImageJ. The primary antibodies used were as follows: anti-actinin (Cell Signaling 6487), anti-OxPhos (Invitrogen 458199) anti-HA (Cell Signaling 14793), anti-IGF2BP2 (MBL RN008P), anti-PBCBP1 (Abcam 74793), anti-PCBP2 (MBL RN250P), anti-SERBP1 (Abcam 55993), anti-TCAP (BD 612328), and anti-MYOM (mMaC myomesin B4 was deposited to the DSHB by Perriard, J.-C.).

Immunofluorescence and RNA FISH

For standard immunofluorescence images, cells were fixed on coverslips (Fisherbrand 12-545-100) in PBS containing 4% paraformaldehyde (EMS 50-980-487) and then permeabilized and blocked in PBS-T (PBS containing 0.1% Triton-X) with 1% BSA (Fisher BP1605100). Cells were probed with primary antibody in PBS-T with BSA overnight at 4°C. The following primary antibodies were used:, anti-Actinin (Sigma A7811) and anti-IGF2BP2 (Bethyl A303-316A). The next day coverslips were washed in PBS-T, incubated for 1 hour at room temperature with 1 µg/mL DAPI (Invitrogen D1306) and appropriate secondary antibody (Invitrogen A-11005 or A-11008) or streptavidin-488 (Invitrogen S11223), washed, and mounted onto slides (Corning 2948) in ProLong Diamond mountant (Invitrogen P36965). An Andor Dragonfly 500 confocal microscope system using a Zyla sCMOS camera and a Leica DMi8 63x oil immersion lens was

used for imaging slides. Andor Fusion software was used to acquire images, which were converted to OME-TIFF format using Bitplane Imaris and analyzed in ImageJ.

ViewRNA direct fluorescence RNA in situ hybridization was conducted using the manufacturer's protocol (Invitrogen 19887). The following human probes were utilized: *NDUFA1* (Invitrogen VA6-3172657), *NDUFA8* (Invitrogen VA1-3003564), *GPX4* (Invitrogen VA1-3000349), and *TTN* (Invitrogen VA6-3173894). Final step of coverslip mounting and image acquisition are described above. For distance quantification, Imaris software was utilized. Images first underwent background subtraction to minimize background signal and allow for clear puncta visualization. The distance transformation tool on Imaris was used to quantify distance (in microns) of RNA puncta and actinin structures.

Mammalian-Two Hybrid

Actinin (full-length and domains), IGF2BP2 (full-length and domains), PCBP1, PBCBP2, and SERBP1 were amplified from human cDNA and cloned into the appropriate vectors (pACT or pBIND) provided by the CheckMate Mammalian Two-Hybrid kit (Promega E2440). The appropriate combination of edited pACT and pBIND vectors, in addition to the kit-provided pGluc5 vector, were transfected using PEI into HEK 293T cells (ATCC CRL-3216), as outlined in the manufacturer's protocol. In addition, the kit-provided positive and negative controls were transfected simultaneously for all experiments to verify proper signal production. Luciferase and Renilla activity were measured using manufacturer's protocol (Promega E1910) utilizing BioTek's Synergy 2 multi-mode microplate reader.

Lentivirus Production

HEK 293T cells (ATCC CRL-3216) were seeded onto 150 mm plates in 20 mL DMEM (Gibco 11965092) supplemented with 10% FBS (Gemini 100-106), GlutaMAX (Gibco 35050061), and 1 mM sodium pyruvate (Gibco 11360070). HEK 293T cells were transfected with 18ug of lentiviral transfer vector, 12 µg psPAX2 (Addgene 12260), and 6 µg pCMV-VSV-G (Addgene 8454). Media was replenished the following day and virus-containing media was harvested at 48, 72,

and 96 hours post-transfection, followed by concentration using PEG-6000 as previously described[59]. For titer determination - iPSCs were transduced with a serial dilution of lentivirus, followed by treating with appropriate antibiotic (1µg/ml puromycin), and counting resistant colony-forming units.

Polysome profiling

IPSC-CMs at day 25 were treated with 0.1 mg/ml cycloheximide at 37 °C for 10 minutes. Cells were washed with 0.1 mg/ml cycloheximide in PBS and lysed in polysome lysis buffer (10 mM HEPES ph7.3, 150 mM KCl, 10 mM $MgCl_2$, 1 mM DTT, 100ug/ml cycloheximide, 2% NP-40, protease inhibitor mini tablet, 6U/ml RNase inhibitor). Samples were kept on ice for 5 minutes during lysis and then centrifuged at 13000g for 10 minutes at 4 °C to remove debris. The BioComp Gradient Station ip Model 153 was used to prepare sucrose gradients. 15% and 50% sucrose solutions (sucrose diluted in 10 mM HEPES pH 7.3, 150 mM KCl, 10 mM $MgCl_2$, 100 ug/ml cycloheximide, 1mM DTT) were utilized. Supernatants from lysed cells were added to sucrose gradients and centrifuged for 150 minutes at 4°C at 120000g (SW41 rotor, Beckman Coulter Optima XPN-100 Ultracentrifuge). BiComp Gradient Station and TRIAX software were utilized for separation of sucrose gradient fractions. Fractions were collected, resuspended in TRIzol and RNA extraction was conducted followed by RNA-Sequencing

Individual Gene Knockdown

Lentiviral-based hairpins were used to individually knockdown genes directly in iPSC-CMs. iPSC-CMs were transduced with lentivirus expressing hairpin at a MOI of 2 in RPMI-B27. Media was replenished the following day and cells were analyzed 7-10 days post transduction.

Flow Cytometry Analysis

BD Biosciences FACSymphony A5 was utilized to perform all flow cytometry experiments. Cells were stained in suspension for 30 minutes at 37°C with 10 µM Hoechst 33342 (Thermo 62249), 200 nM MitoTracker Green (Invitrogen M7514), and 500 nM TO-PRO-3 (Invitrogen T3605). Cells were gated based on forward-scatter and side-scatter, followed by gating of TO-PRO-3 to

identify live cells. Hoechst was used to gate for single cells, followed by subsequent analysis of mitochondrial content (MitoTracker). Final analysis was performed using FlowJo software.

Mito Stress Test

30,000 wildtype CMs were plated on Seahorse XFe96 Cell Culture Microplates (Agilent 101085-004) and lentiviral shRNAs (Scramble and IGF2BP2) were added the next day. The cells were cultured for 7 days before performing the Seahorse XF Cell Mito Stress Test (Agilent 103015-100) according to manufacturer's protocol. The following final concentrations of compounds were injected: oligomycin (1 μM), FCCP (1 μM), and rotenone/antimycin A (0.5 μM).

Cardiac microtissue assay

Cardiac tissues were generated as previously described[20, 21]. Briefly, polydimethylsiloxane (PDMS) (Corning Sylgard 184) cantilever devices were molded from SU-8 masters, which were embedded with fluorescent microbeads (Thermo F8820). Singularized iPSC-CMs were mixed with human cardiac fibroblasts and spun into PDMS devices containing a collagen-based ECM. For knockdown experiments, lentiviral shRNAs were added to iPSC-CMs 7 days prior to generation of tissues. Tissue function was measured once tissues compacted and were visibly pulling the cantilevers. For acquisition of functional data, tissues were stimulated at 1 Hz with a C-Pace EP stimulator (IonOptix) with platinum wire electrodes and fluorescence images were taken at 25 Hz with a Andor Dragonfly microscope equipped with enclosed live-cell chamber (Okolabs). Displacement of fluorescent microbeads was tracked using the ImageJ ParticleTracker plug-in and twitch force was calculated. The cantilever spring constants were determined using the elastic modulus of PDMS and the dimensions of the tissue gauge devices previously described[60].

Statistical Analysis

Obtained data were analyzed in Microsoft Excel and graphed using either GraphPad Prism or R. Data are presented as mean ± standard error of the mean (SEM). Statistical comparisons were conducted via Student's t-test or one-way ANOVA followed by multiple comparisons using

Holm-Sidak correction, where appropriate. Statistical significance was defined by p ≤ 0.05 (*), p ≤ 0.01 (**), p ≤ 0.001 (***), and p ≤ 0.0001 (****).

Extended Data

Figure 1. BioID to establish actinin proximity partners in iPSC-CMs. a) Overview of gene-targeting strategy to generate an in-frame knock-in of BirA*-HA at the *ACTN2* locus in iPSCs. CRISPR/Cas9 and homology-directed repair from a donor vector containing BirA*-HA and 800bp ACTN2 homology arms was utilized. **b)** Actinin-BirA* cardiac microtissues have similar twitch force compared to controls. Data are n≥10 microtissues. (scale bar-150μm). **c)** Representative protein blot probed with streptavidin-HRP to optimize biotin labeling after 24 hours of biotin supplementation up to 50 μM. **d)** Complete STRING network map of Actinin proximity proteins. Data are mean ± SEM; significance assessed by Student's t-test (b) and defined by *P* > 0.05 (ns).

Figure 2. BioID through sarcomere assembly. a) Representative immunoblot of cTnT-KO and cTnT-WT iPSC-CMs lysates probed for cardiac troponin T (cTnT), actinin and GAPDH control. **b)** Representative protein blot of cTnT-KO and cTnT-WT Actinin-BirA* lysates probed with streptavidin-HRP**. c)** FACS quantification of MitoTracker fluorescence intensity in cTnT-KO and WT iPSC-CMs (N>5000 events). **d)** Oxygen consumption rates (OCR) with **e)** parameter quantification of cTnT-KO and cTnT-WT iPSC-CMs. Data are n≥3; mean ± SEM; significance assessed by Student's t-test (c, e) and defined by *P* ≤ 0.01 (**), *P* ≤ 0.001 (***), *P* ≤ 0.0001 (****).

Figure 3. RIP-seq to identify actinin proximity RNA transcripts. a) Heatmap displaying relative expression of ETC Complexes (I-V) genes in Control and Actinin-BirA* RIP-seq samples. **b)** Heatmap displaying relative expression of glycolysis genes in Control vs. Actinin-BirA* RIP-seq samples. **c)** Heatmap displaying relative expression of sarcomere thin and thick filament genes in Control vs. Actinin-BirA* RIP-seq samples. **d)** qPCR validation of candidate

RIP-seq hits. Data are n=4. **e)** RNA FISH of ETC Complex I components NDUFA1 and NDUFA8 that are both in proximity to Actinin but not overlapped (scale bars, main image-10μm, inset-5μm). **f)** Overlap of Actinin-BirA* RIP-seq with Polysome-seq data demonstrates 273 actinin-enriched and translated transcripts. ETC Complex I components are denoted with shaded red circles. **g)** Overlap of Actinin-BirA* RIP-seq with Polysome-seq data demonstrates 87 actinin-depleted and translated transcripts. Sarcomere components are denoted with shaded blue circles. Data are mean ± SEM; significance assessed by Student's t-test (d) and defined by $P \leq 0.01$ (**), $P \leq 0.001$ (***), $P \leq 0.0001$ (****).

Figure 4. RNA-binding proteins interact with actinin. a) Representative immunoblot probed with antibodies to PCPB1, PCPB2 and SERBP1 in streptavidin affinity-purified lysates. **b)** Representative immunoblot probed with antibodies to PCPB1, PCPB2 and SERBP1 in anti-HA immunoprecipitated lysates. **c)** M2H results demonstrating that IGF2BP2 but not PCBP1, PCPB2 and SERBP1 interact with full-length actinin. **d)** Summary overview of RBP and actinin interaction data. **e)** M2H results demonstrating that all actinin isoforms (*ACTN1-4*) interact with IGF2BP2. Data are n=3; mean ± SEM; significance assessed by one-way ANOVA using Holm-Sidak correction for multiple comparisons (c, e) and defined by $P \leq 0.0001$ (****).

Figure 5. IGF2BP2 localizes ETC transcripts to actinin. a) Overview of tandem-IP process (left) and qPCR results of IgG vs. IGF2BP2 IP (right) for candidate ETC transcripts. Data are n=3; mean ± SEM; significance assessed by Student's t-test (a) and defined by $P \leq 0.05$ (*). **b)** Gating strategy utilized for analysis of mitochondrial content for Main Figure 5e.

Table 1. TMT summary data for actinin-proximity proteins. a) Composite protein hits. b) Exp. 1 raw intensity. c) Exp. 2 raw intensity.

Table 2. Actinin-proximity TMT proteins and STRING/GO analyses. a) Protein hits. b) STRING – GO terms. c) STRING – KEGG pathway.

Table 3. Sarcomere assembly-dependent TMT proteins and STRING/GO analyses. a) Protein hits. b) STRING – GO terms. c) STRING – KEGG pathway.

Table 4. RIP-seq data and GO Terms. a) Gene list. b) GO terms (enriched). c) GO terms (depleted).

Table 5. Overlay of RIP-seq and Polysome-seq data and GO terms. a) Combined gene list. b) Gene list for polysome active and RIP enriched. c) GO terms for polysome active and RIP enriched. d) Gene list for polysome active and RIP depleted. e) GO terms for polysome active and RIP depleted.

Table 6. CRISPR and primer sequences.

Movie 1. Control Actinin-BirA* iPSC-CMs paced at 1Hz. Magnification-5X. Scale bar-150μm.

References

1. Liem, R.K. Cytoskeletal Integrators: The Spectrin Superfamily. *Cold Spring Harb Perspect Biol* **8** (2016).
2. Ribeiro Ede, A., Jr. *et al.* The structure and regulation of human muscle alpha-actinin. *Cell* **159**, 1447-1460 (2014).
3. Virel, A. & Backman, L. Molecular evolution and structure of alpha-actinin. *Mol Biol Evol* **21**, 1024-1031 (2004).
4. Murphy, A.C. & Young, P.W. The actinin family of actin cross-linking proteins - a genetic perspective. *Cell Biosci* **5**, 49 (2015).
5. Kunishima, S. *et al.* ACTN1 mutations cause congenital macrothrombocytopenia. *Am J Hum Genet* **92**, 431-438 (2013).
6. Chiu, C. *et al.* Mutations in alpha-actinin-2 cause hypertrophic cardiomyopathy: a genome-wide analysis. *J Am Coll Cardiol* **55**, 1127-1135 (2010).
7. Kaplan, J.M. *et al.* Mutations in ACTN4, encoding alpha-actinin-4, cause familial focal segmental glomerulosclerosis. *Nat Genet* **24**, 251-256 (2000).
8. Chopra, A. *et al.* Force Generation via beta-Cardiac Myosin, Titin, and alpha-Actinin Drives Cardiac Sarcomere Assembly from Cell-Matrix Adhesions. *Dev Cell* **44**, 87-96 e85 (2018).
9. Schultheiss, T. *et al.* A sarcomeric alpha-actinin truncated at the carboxyl end induces the breakdown of stress fibers in PtK2 cells and the formation of nemaline-like bodies and breakdown of myofibrils in myotubes. *Proc Natl Acad Sci U S A* **89**, 9282-9286 (1992).
10. Grison, M., Merkel, U., Kostan, J., Djinovic-Carugo, K. & Rief, M. alpha-Actinin/titin interaction: A dynamic and mechanically stable cluster of bonds in the muscle Z-disk. *Proc Natl Acad Sci U S A* **114**, 1015-1020 (2017).
11. Sanger, J.M. & Sanger, J.W. The dynamic Z bands of striated muscle cells. *Sci Signal* **1**, pe37 (2008).
12. Lange, S., Ehler, E. & Gautel, M. From A to Z and back? Multicompartment proteins in the sarcomere. *Trends Cell Biol* **16**, 11-18 (2006).
13. Djinovic-Carugo, K., Gautel, M., Ylanne, J. & Young, P. The spectrin repeat: a structural platform for cytoskeletal protein assemblies. *FEBS Lett* **513**, 119-123 (2002).
14. Foley, K.S. & Young, P.W. The non-muscle functions of actinins: an update. *Biochem J* **459**, 1-13 (2014).
15. Roux, K.J., Kim, D.I., Raida, M. & Burke, B. A promiscuous biotin ligase fusion protein identifies proximal and interacting proteins in mammalian cells. *J Cell Biol* **196**, 801-810 (2012).
16. Gingras, A.C., Abe, K.T. & Raught, B. Getting to know the neighborhood: using proximity-dependent biotinylation to characterize protein complexes and map organelles. *Curr Opin Chem Biol* **48**, 44-54 (2019).
17. Kim, D.I. *et al.* Probing nuclear pore complex architecture with proximity-dependent biotinylation. *Proc Natl Acad Sci U S A* **111**, E2453-2461 (2014).
18. Tohyama, S. *et al.* Distinct metabolic flow enables large-scale purification of mouse and human pluripotent stem cell-derived cardiomyocytes. *Cell Stem Cell* **12**, 127-137 (2013).
19. Lian, X. *et al.* Robust cardiomyocyte differentiation from human pluripotent stem cells via temporal modulation of canonical Wnt signaling. *Proc Natl Acad Sci U S A* **109**, E1848-1857 (2012).

20. Hinson, J.T. *et al.* HEART DISEASE. Titin mutations in iPS cells define sarcomere insufficiency as a cause of dilated cardiomyopathy. *Science* **349**, 982-986 (2015).
21. Cohn, R. *et al.* A Contraction Stress Model of Hypertrophic Cardiomyopathy due to Sarcomere Mutations. *Stem Cell Reports* **12**, 71-83 (2019).
22. Auerbach, D. *et al.* Different domains of the M-band protein myomesin are involved in myosin binding and M-band targeting. *Mol Biol Cell* **10**, 1297-1308 (1999).
23. Gautel, M. & Djinovic-Carugo, K. The sarcomeric cytoskeleton: from molecules to motion. *J Exp Biol* **219**, 135-145 (2016).
24. Hayashi, T. *et al.* Tcap gene mutations in hypertrophic cardiomyopathy and dilated cardiomyopathy. *J Am Coll Cardiol* **44**, 2192-2201 (2004).
25. Lyon, R.C., Zanella, F., Omens, J.H. & Sheikh, F. Mechanotransduction in cardiac hypertrophy and failure. *Circ Res* **116**, 1462-1476 (2015).
26. Szklarczyk, D. *et al.* STRING v11: protein-protein association networks with increased coverage, supporting functional discovery in genome-wide experimental datasets. *Nucleic Acids Res* **47**, D607-D613 (2019).
27. Faulkner, G. *et al.* FATZ, a filamin-, actinin-, and telethonin-binding protein of the Z-disc of skeletal muscle. *J Biol Chem* **275**, 41234-41242 (2000).
28. Crawford, A.W., Michelsen, J.W. & Beckerle, M.C. An interaction between zyxin and alpha-actinin. *J Cell Biol* **116**, 1381-1393 (1992).
29. Nieset, J.E. *et al.* Characterization of the interactions of alpha-catenin with alpha-actinin and beta-catenin/plakoglobin. *J Cell Sci* **110 (Pt 8)**, 1013-1022 (1997).
30. Du, A., Sanger, J.M., Linask, K.K. & Sanger, J.W. Myofibrillogenesis in the first cardiomyocytes formed from isolated quail precardiac mesoderm. *Dev Biol* **257**, 382-394 (2003).
31. Nishii, K. *et al.* Targeted disruption of the cardiac troponin T gene causes sarcomere disassembly and defects in heartbeat within the early mouse embryo. *Dev Biol* **322**, 65-73 (2008).
32. Knoll, R. *et al.* The cardiac mechanical stretch sensor machinery involves a Z disc complex that is defective in a subset of human dilated cardiomyopathy. *Cell* **111**, 943-955 (2002).
33. Heineke, J. *et al.* Attenuation of cardiac remodeling after myocardial infarction by muscle LIM protein-calcineurin signaling at the sarcomeric Z-disc. *Proc Natl Acad Sci U S A* **102**, 1655-1660 (2005).
34. Knoll, R. *et al.* A common MLP (muscle LIM protein) variant is associated with cardiomyopathy. *Circ Res* **106**, 695-704 (2010).
35. Tenenbaum, S.A., Carson, C.C., Lager, P.J. & Keene, J.D. Identifying mRNA subsets in messenger ribonucleoprotein complexes by using cDNA arrays. *Proc Natl Acad Sci U S A* **97**, 14085-14090 (2000).
36. Pringle, E.S., McCormick, C. & Cheng, Z. Polysome Profiling Analysis of mRNA and Associated Proteins Engaged in Translation. *Curr Protoc Mol Biol* **125**, e79 (2019).
37. Diabetes Genetics Initiative of Broad Institute of, H. *et al.* Genome-wide association analysis identifies loci for type 2 diabetes and triglyceride levels. *Science* **316**, 1331-1336 (2007).
38. Ryu, M.S., Zhang, D., Protchenko, O., Shakoury-Elizeh, M. & Philpott, C.C. PCBP1 and NCOA4 regulate erythroid iron storage and heme biosynthesis. *J Clin Invest* **127**, 1786-1797 (2017).

39. Frey, A.G. *et al.* Iron chaperones PCBP1 and PCBP2 mediate the metallation of the dinuclear iron enzyme deoxyhypusine hydroxylase. *Proc Natl Acad Sci U S A* **111**, 8031-8036 (2014).
40. Muto, A. *et al.* The mRNA-binding protein Serbp1 as an auxiliary protein associated with mammalian cytoplasmic ribosomes. *Cell Biochem Funct* **36**, 312-322 (2018).
41. Janiszewska, M. *et al.* Imp2 controls oxidative phosphorylation and is crucial for preserving glioblastoma cancer stem cells. *Genes Dev* **26**, 1926-1944 (2012).
42. Suga, H. Ventricular energetics. *Physiol Rev* **70**, 247-277 (1990).
43. Frey, N. & Olson, E.N. Calsarcin-3, a novel skeletal muscle-specific member of the calsarcin family, interacts with multiple Z-disc proteins. *J Biol Chem* **277**, 13998-14004 (2002).
44. Faulkner, G. *et al.* ZASP: a new Z-band alternatively spliced PDZ-motif protein. *J Cell Biol* **146**, 465-475 (1999).
45. Arber, S. *et al.* MLP-deficient mice exhibit a disruption of cardiac cytoarchitectural organization, dilated cardiomyopathy, and heart failure. *Cell* **88**, 393-403 (1997).
46. Chowrashi, P., Mittal, B., Sanger, J.M. & Sanger, J.W. Amorphin is phosphorylase; phosphorylase is an alpha-actinin-binding protein. *Cell Motil Cytoskeleton* **53**, 125-135 (2002).
47. Rakus, D., Mamczur, P., Gizak, A., Dus, D. & Dzugaj, A. Colocalization of muscle FBPase and muscle aldolase on both sides of the Z-line. *Biochem Biophys Res Commun* **311**, 294-299 (2003).
48. Branon, T.C. *et al.* Efficient proximity labeling in living cells and organisms with TurboID. *Nat Biotechnol* **36**, 880-887 (2018).
49. Lecuyer, E. *et al.* Global analysis of mRNA localization reveals a prominent role in organizing cellular architecture and function. *Cell* **131**, 174-187 (2007).
50. Martin, K.C. & Ephrussi, A. mRNA localization: gene expression in the spatial dimension. *Cell* **136**, 719-730 (2009).
51. Boncompagni, S. *et al.* Mitochondria are linked to calcium stores in striated muscle by developmentally regulated tethering structures. *Mol Biol Cell* **20**, 1058-1067 (2009).
52. Ferreira, R. *et al.* Subsarcolemmal and intermyofibrillar mitochondria proteome differences disclose functional specializations in skeletal muscle. *Proteomics* **10**, 3142-3154 (2010).
53. Regue, L. *et al.* IMP2 Increases Mouse Skeletal Muscle Mass and Voluntary Activity by Enhancing Autocrine Insulin-Like Growth Factor 2 Production and Optimizing Muscle Metabolism. *Mol Cell Biol* **39** (2019).
54. Lian, X. *et al.* Directed cardiomyocyte differentiation from human pluripotent stem cells by modulating Wnt/beta-catenin signaling under fully defined conditions. *Nat Protoc* **8**, 162-175 (2013).
55. Irie, N. *et al.* SOX17 is a critical specifier of human primordial germ cell fate. *Cell* **160**, 253-268 (2015).
56. Gafni, O. *et al.* Derivation of novel human ground state naive pluripotent stem cells. *Nature* **504**, 282-286 (2013).
57. Ong, S.E. *et al.* Stable isotope labeling by amino acids in cell culture, SILAC, as a simple and accurate approach to expression proteomics. *Mol Cell Proteomics* **1**, 376-386 (2002).

58. McAlister, G.C. *et al.* MultiNotch MS3 enables accurate, sensitive, and multiplexed detection of differential expression across cancer cell line proteomes. *Anal Chem* **86**, 7150-7158 (2014).
59. Kutner, R.H., Zhang, X.Y. & Reiser, J. Production, concentration and titration of pseudotyped HIV-1-based lentiviral vectors. *Nat Protoc* **4**, 495-505 (2009).
60. Boudou, T. *et al.* A microfabricated platform to measure and manipulate the mechanics of engineered cardiac microtissues. *Tissue Eng Part A* **18**, 910-919 (2012).

Figure 1

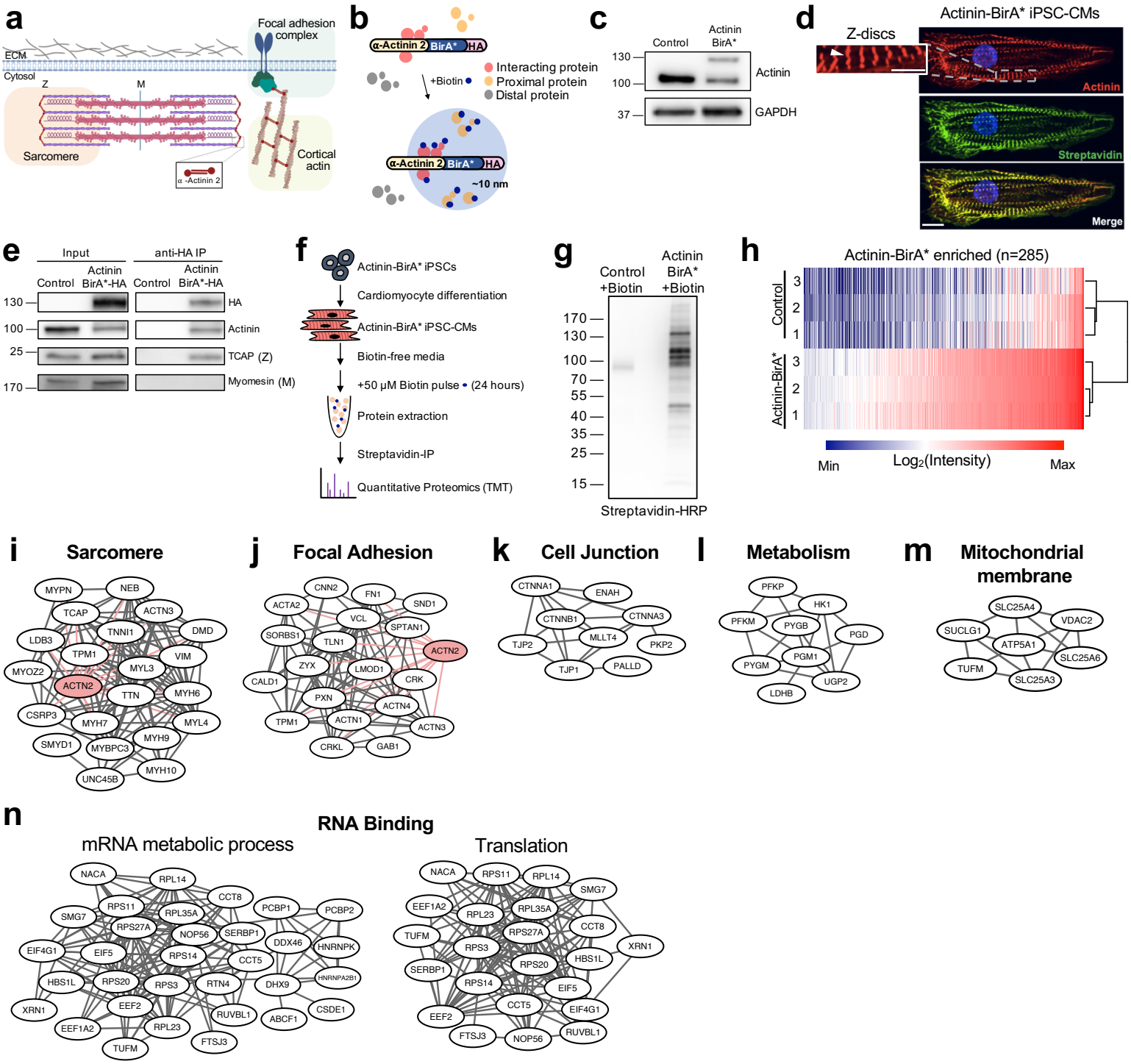
a
Focal adhesion complex
ECM
Cytosol
Z
M
Sarcomere
Cortical actin
α -Actinin 2
b
α-Actinin 2
BirA*
HA
+Biotin
Interacting protein
Proximal protein
Distal protein
~10 nm
c
Control
Actinin BirA*
130
100
37
Actinin
GAPDH
d
Actinin-BirA* iPSC-CMs
Z-discs
Actinin
Streptavidin
Merge
e
Input
anti-HA IP
Control
Actinin BirA*-HA
130
100
25
170
HA
Actinin
TCAP (Z)
Myomesin (M)
f
Actinin-BirA* iPSCs
Cardiomyocyte differentiation
Actinin-BirA* iPSC-CMs
Biotin-free media
+50 μM Biotin pulse (24 hours)
Protein extraction
Streptavidin-IP
Quantitative Proteomics (TMT)
g
Control +Biotin
Actinin BirA* +Biotin
170
130
100
70
55
40
35
25
15
Streptavidin-HRP
h
Actinin-BirA* enriched (n=285)
Control
Actinin-BirA*
3
2
1
Min
Log2(Intensity)
Max
i
Sarcomere
MYPN
NEB
TCAP
ACTN3
LDB3
TNNI1
DMD
TPM1
VIM
MYOZ2
MYL3
ACTN2
TTN
MYH6
CSRP3
MYH7
MYL4
SMYD1
MYH9
MYBPC3
MYH10
UNC45B
j
Focal Adhesion
CNN2
FN1
SND1
ACTA2
VCL
SPTAN1
SORBS1
TLN1
ACTN2
ZYX
LMOD1
CALD1
CRK
PXN
ACTN4
TPM1
ACTN1
ACTN3
CRKL
GAB1
k
Cell Junction
CTNNA1
ENAH
CTNNB1
CTNNA3
TJP2
MLLT4
PKP2
TJP1
PALLD
l
Metabolism
PFKP
HK1
PFKM
PYGB
PGD
PGM1
PYGM
UGP2
LDHB
m
Mitochondrial membrane
SLC25A4
VDAC2
SUCLG1
ATP5A1
SLC25A6
TUFM
SLC25A3
n
RNA Binding
mRNA metabolic process
NACA
RPL14
CCT8
RPS11
RPL35A
PCBP1
PCBP2
SMG7
RPS27A
NOP56
SERBP1
DDX46
HNRNPK
EIF4G1
EIF5
RPS14
CCT5
HNRNPA2B1
HBS1L
RPS20
RPS3
RTN4
DHX9
XRN1
EEF2
RUVBL1
CSDE1
ABCF1
EEF1A2
RPL23
FTSJ3
TUFM
Translation
NACA
RPS11
RPL14
SMG7
EEF1A2
RPL23
RPL35A
TUFM
RPS27A
CCT8
RPS3
XRN1
SERBP1
RPS20
HBS1L
RPS14
EIF5
CCT5
EIF4G1
EEF2
FTSJ3
NOP56
RUVBL1

Figure 2

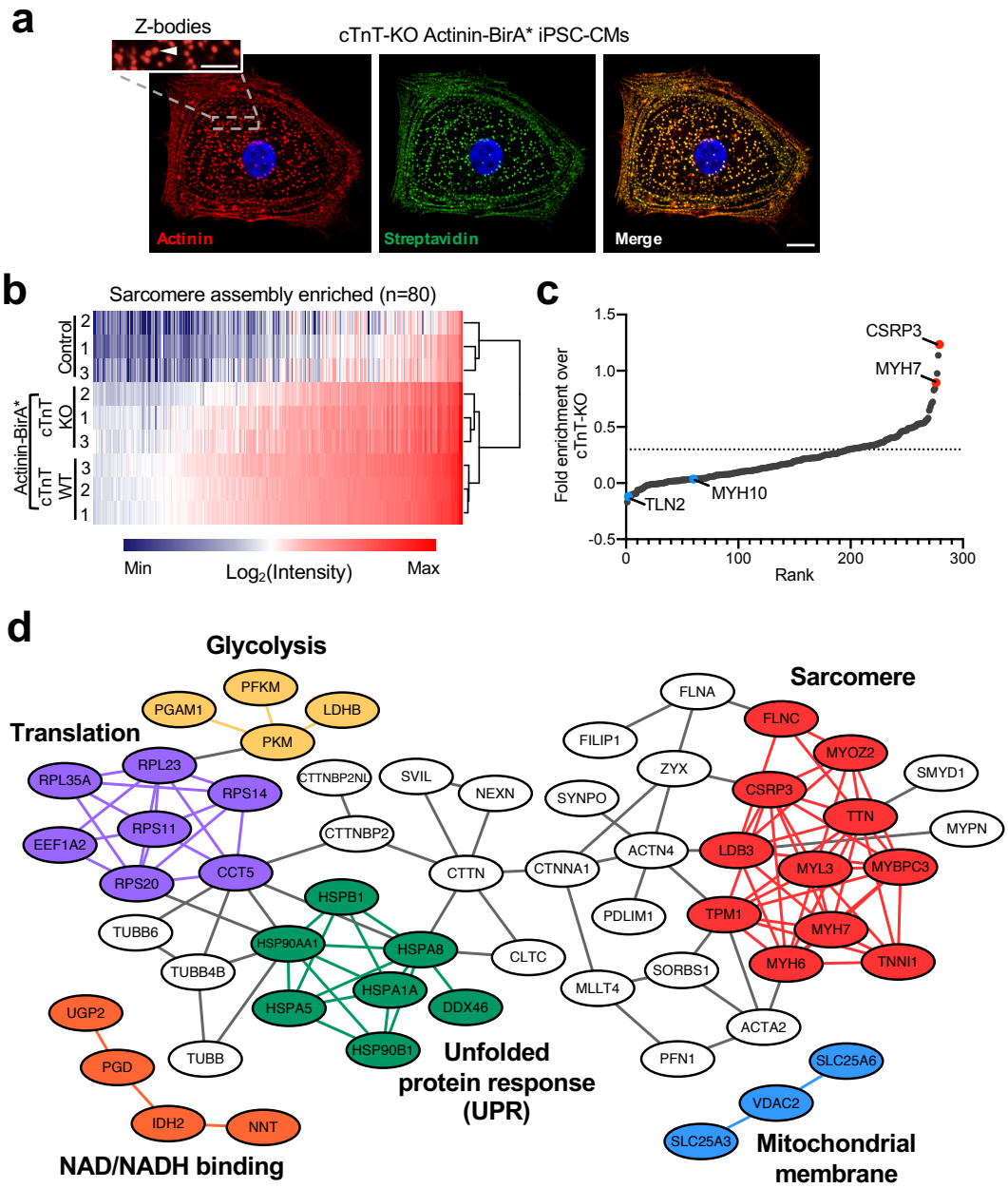
a
Z-bodies
cTnT-KO Actinin-BirA* iPSC-CMs
Actinin
Streptavidin
Merge
b
Sarcomere assembly enriched (n=80)
Control
Actinin-BirA*
cTnT KO
cTnT WT
Min
Log2(Intensity)
Max
c
Fold enrichment over cTnT-KO
Rank
CSRP3
MYH7
MYH10
TLN2
d
Glycolysis
PFKM
PGAM1
LDHB
PKM
Translation
RPL23
RPL35A
RPS14
RPS11
EEF1A2
RPS20
CCT5
TUBB6
TUBB4B
TUBB
UGP2
PGD
IDH2
NNT
NAD/NADH binding
CTTNBP2NL
SVIL
NEXN
CTTNBP2
CTTN
HSPB1
HSP90AA1
HSPA8
HSPA1A
HSPA5
DDX46
HSP90B1
Unfolded protein response (UPR)
CLTC
SYNPO
CTNNA1
ACTN4
PDLIM1
MLLT4
SORBS1
PFN1
ACTA2
Sarcomere
FLNA
FLNC
FILIP1
ZYX
MYOZ2
SMYD1
CSRP3
TTN
MYPN
LDB3
MYL3
MYBPC3
TPM1
MYH7
MYH6
TNNI1
SLC25A6
VDAC2
SLC25A3
Mitochondrial membrane

Figure 3

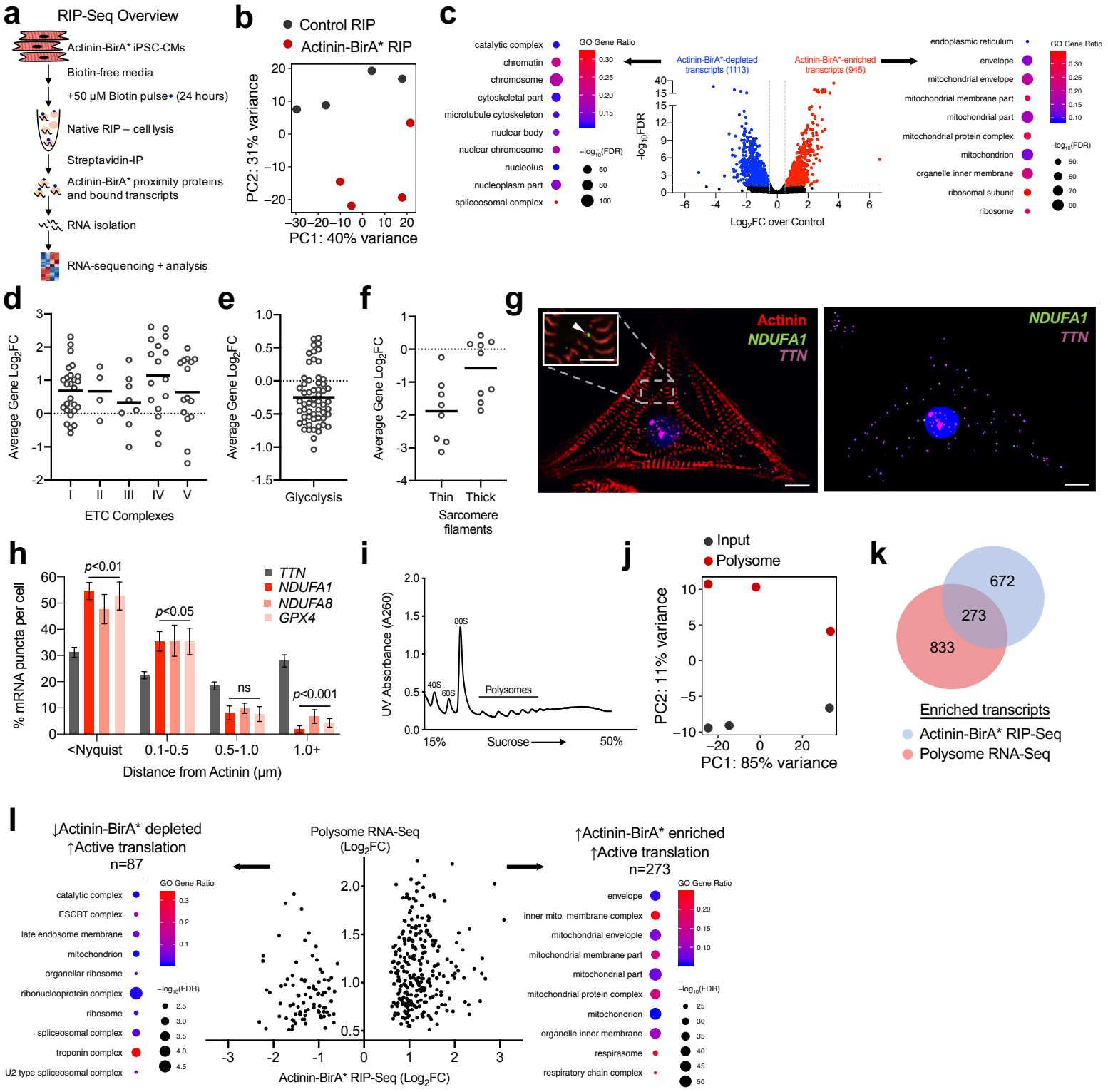
a
RIP-Seq Overview
Actinin-BirA* iPSC-CMs
Biotin-free media
+50 µM Biotin pulse (24 hours)
Native RIP – cell lysis
Streptavidin-IP
Actinin-BirA* proximity proteins and bound transcripts
RNA isolation
RNA-sequencing + analysis
b
Control RIP
Actinin-BirA* RIP
PC2: 31% variance
PC1: 40% variance
c
Actinin-BirA*-depleted transcripts (1113)
Actinin-BirA*-enriched transcripts (945)
Log2FC over Control
-log10FDR
GO Gene Ratio
catalytic complex
chromatin
chromosome
cytoskeletal part
microtubule cytoskeleton
nuclear body
nuclear chromosome
nucleolus
nucleoplasm part
spliceosomal complex
endoplasmic reticulum
envelope
mitochondrial envelope
mitochondrial membrane part
mitochondrial part
mitochondrial protein complex
mitochondrion
organelle inner membrane
ribosomal subunit
ribosome
d
Average Gene Log2FC
ETC Complexes
e
Glycolysis
f
Thin
Thick
Sarcomere filaments
g
Actinin
NDUFA1
TTN
h
p<0.01
p<0.05
ns
p<0.001
TTN
NDUFA1
NDUFA8
GPX4
% mRNA puncta per cell
<Nyquist
0.1-0.5
0.5-1.0
1.0+
Distance from Actinin (µm)
i
UV Absorbance (A260)
40S
60S
80S
Polysomes
15%
Sucrose
50%
j
Input
Polysome
PC2: 11% variance
PC1: 85% variance
k
672
273
833
Enriched transcripts
Actinin-BirA* RIP-Seq
Polysome RNA-Seq
l
↓Actinin-BirA* depleted
↑Active translation
n=87
catalytic complex
ESCRT complex
late endosome membrane
mitochondrion
organellar ribosome
ribonucleoprotein complex
ribosome
spliceosomal complex
troponin complex
U2 type spliceosomal complex
Polysome RNA-Seq (Log2FC)
Actinin-BirA* RIP-Seq (Log2FC)
↑Actinin-BirA* enriched
↑Active translation
n=273
envelope
inner mito. membrane complex
mitochondrial envelope
mitochondrial membrane part
mitochondrial part
mitochondrial protein complex
mitochondrion
organelle inner membrane
respirasome
respiratory chain complex

Figure 4

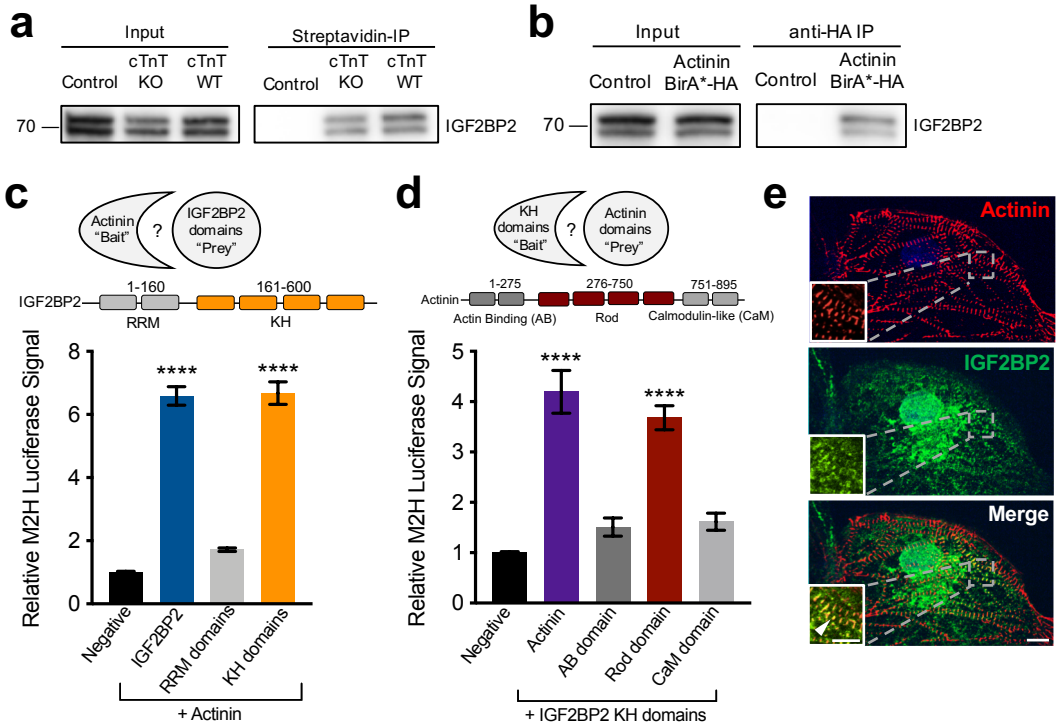
a
Input
Control
cTnT KO
cTnT WT
Streptavidin-IP
Control
cTnT KO
cTnT WT
70
IGF2BP2
b
Input
Control
Actinin BirA*-HA
anti-HA IP
Control
Actinin BirA*-HA
70
IGF2BP2
c
Actinin "Bait"
?
IGF2BP2 domains "Prey"
IGF2BP2
1-160
161-600
RRM
KH
Relative M2H Luciferase Signal
****
****
Negative
IGF2BP2
RRM domains
KH domains
+ Actinin
d
KH domains "Bait"
?
Actinin domains "Prey"
Actinin
1-275
276-750
751-895
Actin Binding (AB)
Rod
Calmodulin-like (CaM)
Relative M2H Luciferase Signal
****
****
Negative
Actinin
AB domain
Rod domain
CaM domain
+ IGF2BP2 KH domains
e
Actinin
IGF2BP2
Merge

Figure 5

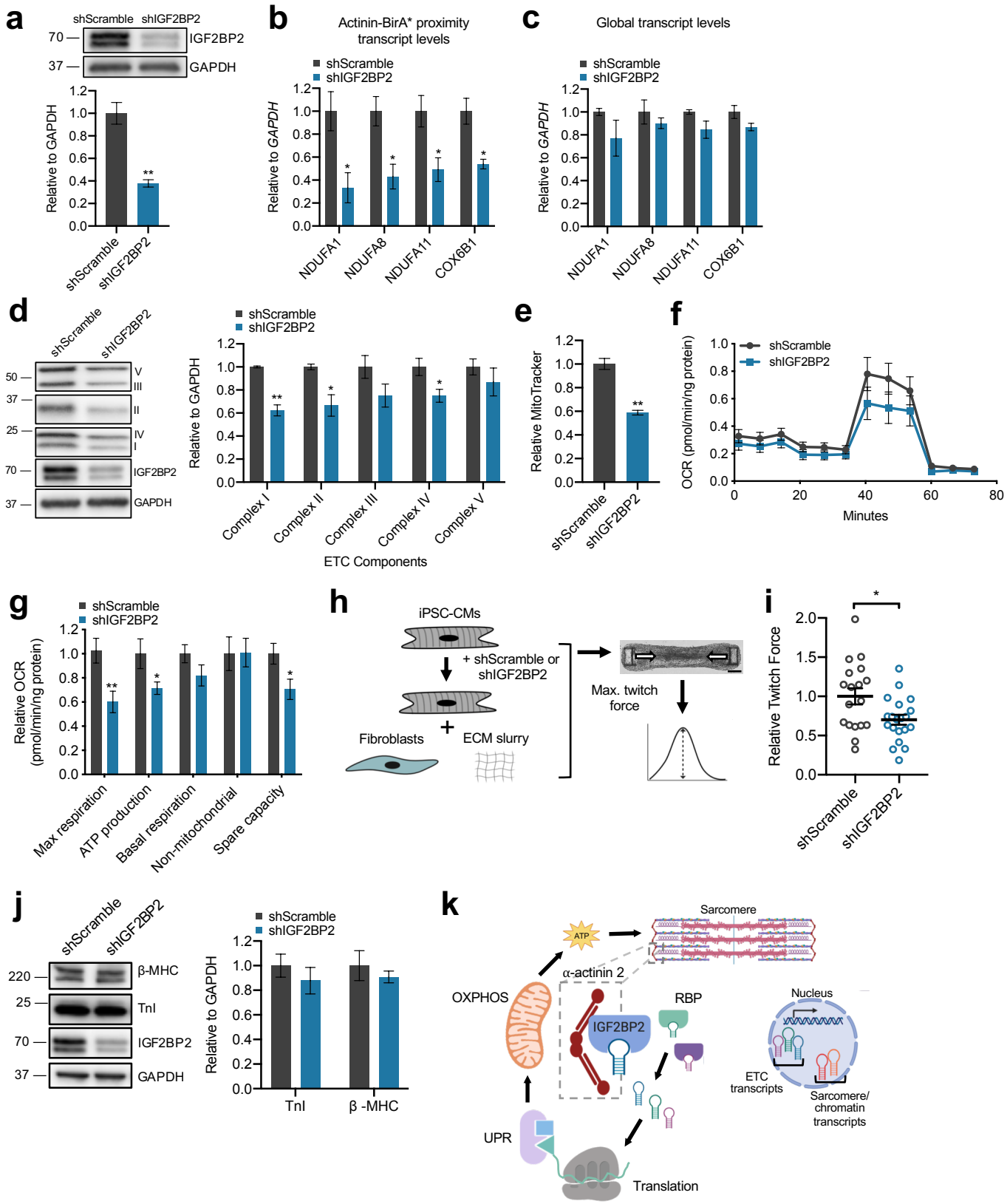
a
shScramble
shIGF2BP2
70
37
IGF2BP2
GAPDH
Relative to GAPDH
b
Actinin-BirA* proximity transcript levels
shScramble
shIGF2BP2
Relative to GAPDH
NDUFA1
NDUFA8
NDUFA11
COX6B1
c
Global transcript levels
d
50
37
25
V
III
II
IV
I
Complex I
Complex II
Complex III
Complex IV
Complex V
ETC Components
e
Relative MitoTracker
f
OCR (pmol/min/ng protein)
Minutes
g
Relative OCR (pmol/min/ng protein)
Max respiration
ATP production
Basal respiration
Non-mitochondrial
Spare capacity
h
iPSC-CMs
+ shScramble or shIGF2BP2
Fibroblasts
ECM slurry
Max. twitch force
i
Relative Twitch Force
j
220
β-MHC
TnI
β -MHC
k
Sarcomere
ATP
α-actinin 2
OXPHOS
RBP
Nucleus
ETC transcripts
Sarcomere/ chromatin transcripts
UPR
Translation

Extended data 1

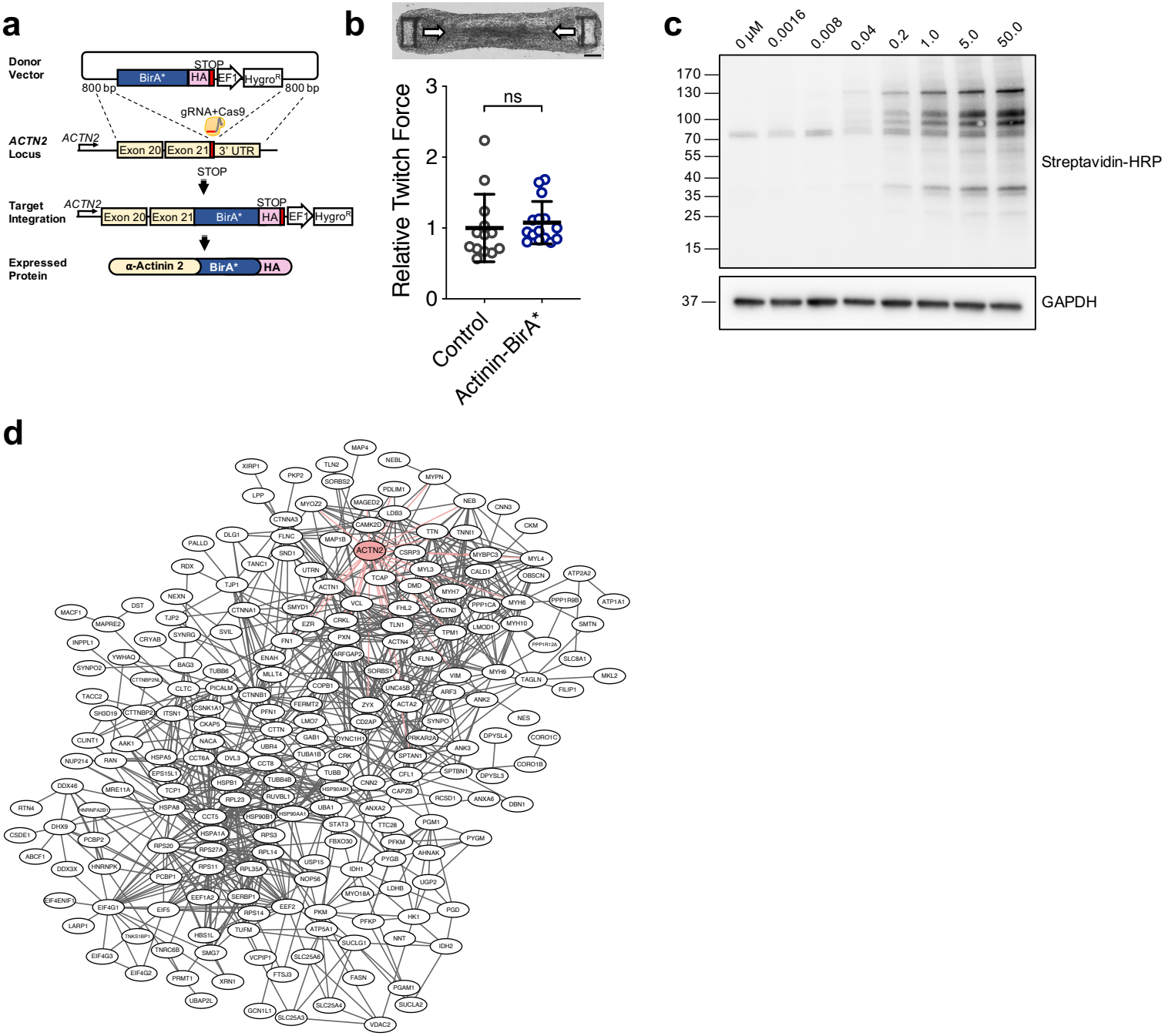

Extended data 2

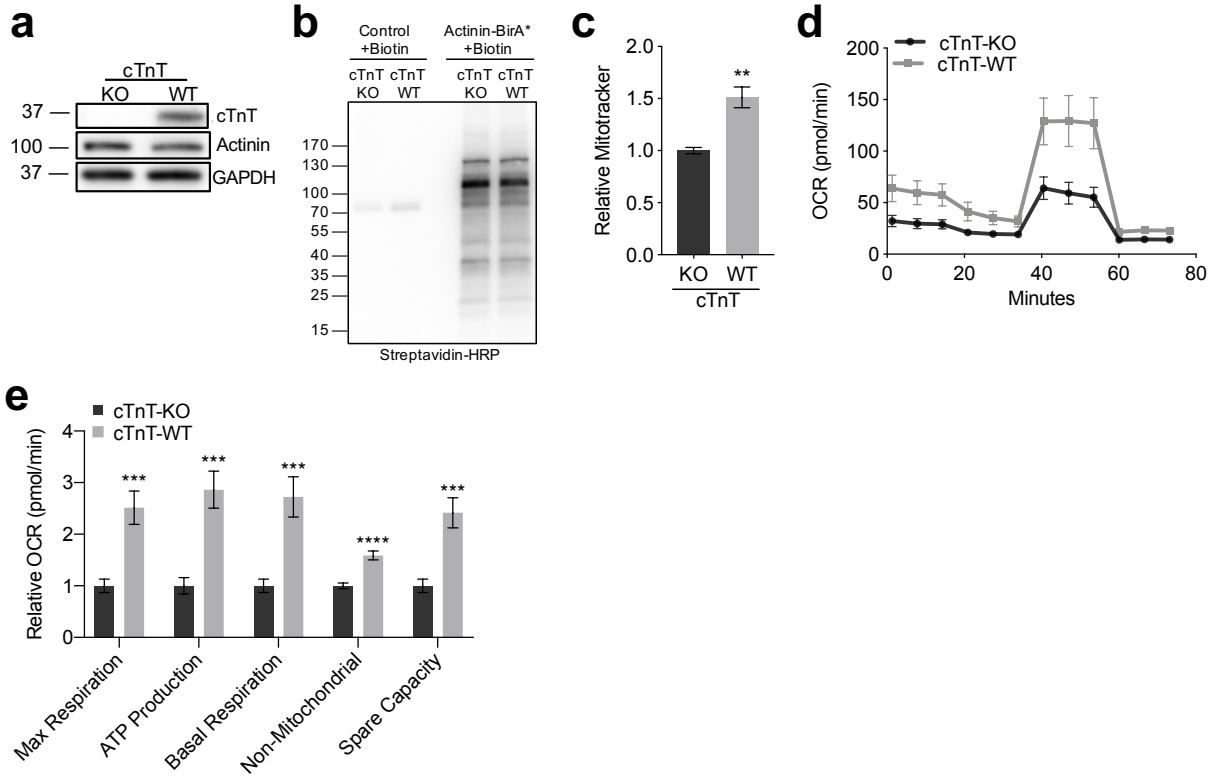

Extended data 3

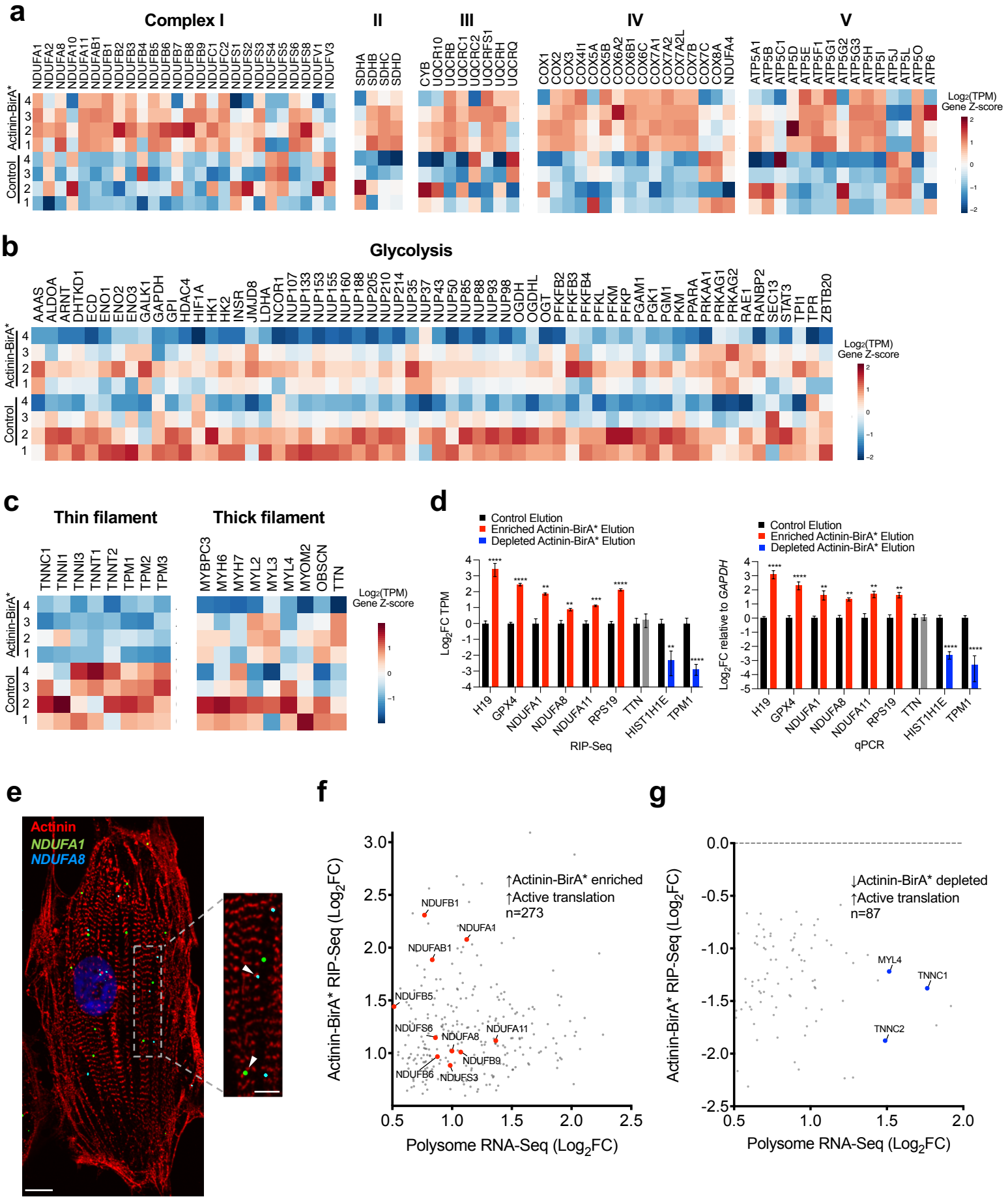

Extended data 4

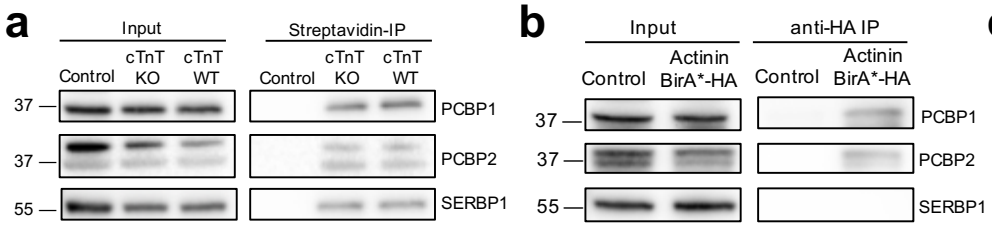

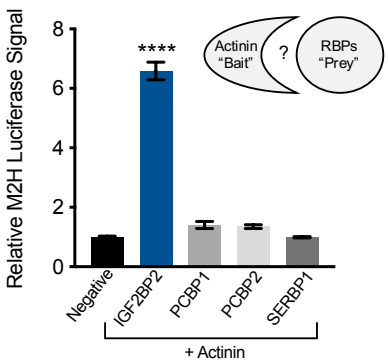

d

RNA Binding Protein	Method			
	TMT	SP-IP	HA-IP	M2H
IGF2BP2	+	+	+	+
PCBP1	+	+	+	-
PCBP2	+	+	+	-
SERBP1	+	+	-	-

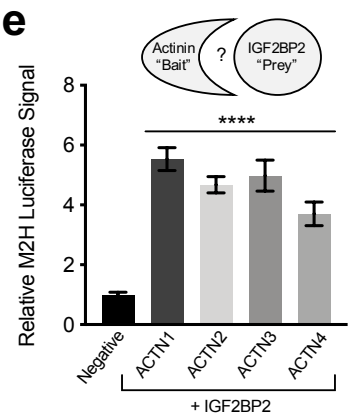

Extended data 5

a

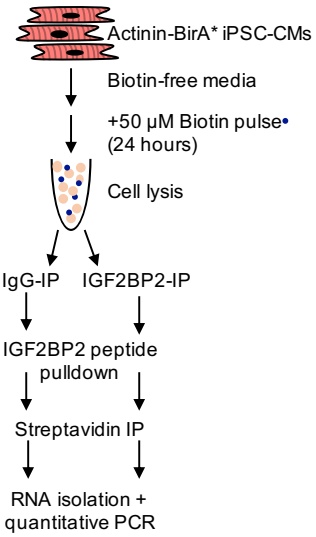

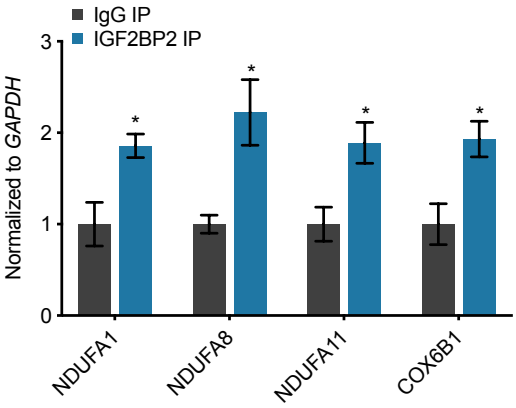
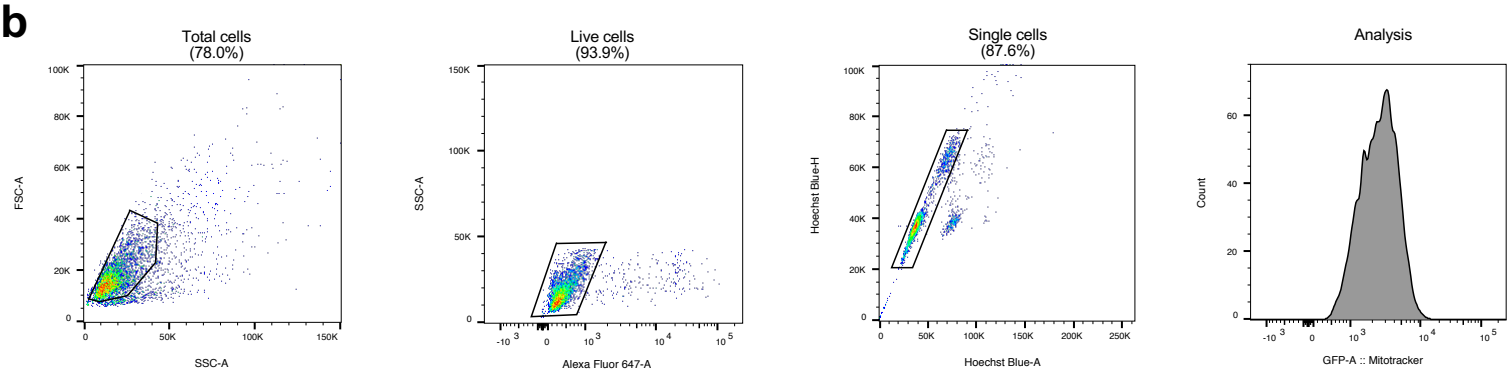
b